日本磁気学会
ISSN 2432-0250
Journal of the Magnetics Society of Japan
Electronic Journal URL: https://www.jstage.jst.go.jp/browse/msjmag

Vol.43 No.6 2019

Journal

JOURNAL OF THE MAGNETICS SOCIETY OF JAPAN

Vol.43 No.6 2019

日本磁気学会

ISSN 2432-0250

HP: http://www.magnetics.jp/ e-mail: msj@bj.wakwak.com
Electronic Journal: http://www.jstage.jst.go.jp/browse/msjmag

Journal of the Magnetics Society of Japan
Vol. 43, No. 6

Electronic Journal URL: https://www.jstage.jst.go.jp/browse/msjmag

CONTENTS

J. Magn. Soc. Jpn., **43**, 105-108 (2019)

Letter

Representation of Magnetic Hysteresis Phenomena under Inverter Excitation in a Circuit Simulator using Coupling Analysis of Electricity and Magnetism

A. Yao, T. Funaki*, and T. Hatakeyama
Department of Electrical and Computer Engineering, Toyama Prefectural University, *5180, Kurokawa, Imizu 939-0398, Japan*
*Division of Electrical, Electronic and Information Engineering, Osaka University, *2-1, Yamadaoka, Suita, Osaka 565-0781, Japan*

We focus on accurate representations of hysteretic phenomena under pulse width modulation (PWM) inverter excitation using strong-coupling analysis of the magnetic field and the electric circuit. We perform the strong-coupling analysis by applying a dynamic hysteresis model (play model with the Cauer circuit) to a circuit simulator. We show that, by accounting for dead time properties, the numerical voltage waveforms obtained in our study are consistent with those obtained experimentally. Further, the accurate representations of the voltage waveform and of the high and wide band frequency indicate that the hysteresis curves simulated by our proposed strong-coupling analysis agree well with the measured results.

Key words: hysteresis property, inverter, Cauer circuit, play model, iron loss

1 Introduction

Pulse width modulation (PWM) excitation is generally used for speed control in motor drive systems. Many studies have shown that high frequency components under PWM excitation induce complex dynamic hysteretic magnetic curves in soft magnetic materials (*e.g.* motor core)[1–11]. The iron losses of the magnetic core under PWM inverter excitation increase by 10%-50% compared to those under sinusoidal excitation due to the high order harmonic components[5]. It is important to accurately simulate the dynamic hysteretic curves of soft magnetic materials to achieve the highly accurate loss estimation of motor drive systems. Recently, several researchers focused on expressing hysteretic phenomena under PWM inverter excitation using numerical simulations. Some studies have addressed the play model[12–14] with the Cauer circuit[15–22] to express the nonlinear hysteretic properties. The play model with the Cauer circuit allows to accurately represent hysteretic curves without the use of sub-analysis methods[17,19].

It is known that power semiconductor, dead time, and ringing properties in the inverter affect the hysteresis and iron loss properties of magnetic materials[5,22–25]. Recently, Odawara *et al.* reported the simulation of the hysteretic curves using the play model with the Cauer circuit and accounting for power semiconductor properties[18,21]. They achieved a weak-coupling analysis, in which the magnetic field and the electric circuit are separately solved. This calculation included only $I-V$ properties of the semiconductors. The next phase is to perform a strong-coupling analysis (electrical and magnetic properties are simultaneously solved) that considers not only $I-V$ properties of the semiconductors but also the change in the output of the inverter due to dead time, the rising and falling waveforms of voltage and current, the ringing, and so on. The goal of the work presented in this study is to develop the strong-coupling analysis method with a circuit simulator.

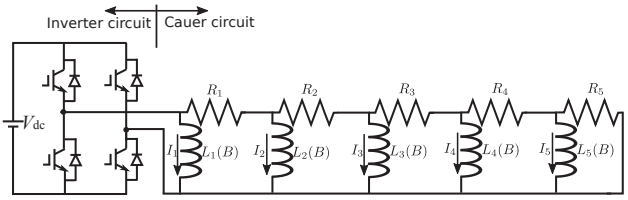

Fig. 1 Schematic diagram for strong-coupling analysis of inverter circuit and hysteresis model (play model with Cauer circuit) in circuit simulator. Cauer circuit corresponds to *RL* ladder circuit. Here, the figure shows the 5-stage *RL* ladder circuit. I_n is calculated based on the play model with Eq. (4).

This study focuses on expressing hysteretic phenomena of magnetic materials under PWM inverter excitation using the strong-coupling analysis of the magnetic field and the electric circuit. The dynamic hysteresis model (play model with the Cauer circuit) is implemented in a circuit simulator (PSIM, Powersim). The reset of this paper is organized as follows: We perform a highly accurate simulation by considering dead time properties in the strong-coupling analysis. Next, we discuss the accurate expression of magnetic hysteresis properties for the high and wide band frequency by increasing the number of stages in the Cauer circuit and by calculating the current based on the play model.

2 Method

We use a ring core composed of laminated standard non-oriented electrical (NO) steel sheets (35H300) to obtain the experimental hysteresis properties of magnetic materials under PWM inverter excitation. This study uses an inverter (PM75RSD060, Mitsubishi Electric Corporation), a high performance analog-to-digital (A/D) converter (PXI-5122, National Instruments), a current probe (SS-250, Iwatsu), and a voltage probe (SS-320, Iwatsu) to experimentally measure hysteresis properties. The iron loss W_{fe} of the ring core is formulated by

using magnetic field intensity H and magnetic flux density B as [20,24]

$$W_{\mathrm{fe}} = \frac{1}{T\rho}\int H\mathrm{d}B, \tag{1}$$

$$H = \frac{N_1 I}{l}, \tag{2}$$

$$B = \frac{1}{N_2 S}\int V dt, \tag{3}$$

where ρ (= 7650 kg/m^3) denotes the density of NO sheets, T (= 0.02 s) is the period of the fundamental wave, I is the current flowing in the primary coil of the ring core, V is the induced voltage of the secondary coil, N_1 (= 264) is the number of turns of the primary coil, N_2 (= 264) is the number of turns of the secondary coil, l (= 0.36 m) is the average magnetic path length, and S (= 87.5 mm^2) is the cross section area of the core (See Refs.[20,24] for details of the ring tests.).

We implement a dynamic hysteresis model in the circuit simulator (PSIM, Powersim) to simulate magnetic hysteresis phenomena under PWM inverter excitation using the strong-coupling analysis method. Figure 1 shows a schematic circuit diagram for the strong-coupling analysis method of the inverter circuit and the hysteresis model. The circuit simulator used in this study can consider $I-V$, dead time, and switching properties of the inverter and calculate the dynamic hysteretic model of magnetic materials. Then, we can perform the coupling analysis of electricity and magnetism. In our numerical simulations, the dynamic hysteresis model consists of the play model and the Cauer circuit to express the DC and the AC components of the hysteresis curves, respectively. The previous study carried out the calculation including only $I-V$ properties of the semiconductors[18,21]. In other words, the effects of dead time, the rising and falling waveforms, the ringing, and so on were neglected[18,21].

Based on previous studies[17,19–21], in our numerical simulations, the current I_n through the n-th nonlinear inductor $L_n(B)$ and the equivalent resistance R_n in the magnetic analysis to represent eddy current loss are calculated by

$$I_n = \frac{l}{N_1}H_{\mathrm{DC}}((4n-3)B_n), \tag{4}$$

$$R_n = \frac{N_1 N_2 S}{l}(4n-1)\frac{12}{\alpha\sigma d^2}, \tag{5}$$

where $H_{\mathrm{DC}}((4n-3)B_n)$ denotes the DC hysteretic property represented by the play model[19,20] at $L_n(B)$, d (=0.35 mm) is the thickness of the NO sheet, σ (=1.923 $\times$ 10^6 S/m) is the electrical conductivity of the NO sheet, and α is the anomaly factor to express anomaly eddy currents[20]. See Refs.[17–21] for details of numerical methods based on the play model with the Cauer circuit.

The Cauer circuit comprises RL ladder circuits. In the Cauer circuit, the number of sets of R and L restricts the expression of the high and wide band frequency for the numerical hysteretic curves. Here, the Cauer circuit with 2-, 3-, 4-, and 5-stage RL ladder circuits can well express the dynamic hysteresis curves up to about 30, 100, 400, and 1000 kHz, respectively. See Ref.[26] for details of the frequency limit for the accurate representations of hysteresis curves.

Our numerical method (the strong-coupling analysis) with the circuit simulator does not, in principle, have the frequency limit for expressing the numerical hysteretic curves because it is easy to add the RL ladder circuit of the Cauer circuit in the circuit simulator. However, the previous study is limited to the Cauer circuit with the 3-stage RL ladder circuit[21] because it is necessary to solve the magnetic equation analytically. The previous method[21] is difficult to calculate the hysteretic properties for the high and wide band frequencies. Therefore, our numerical method with multi-stage (four or more stages) RL ladder circuit is useful for performing calculations in high and wide band frequency region. Our paper compares the results of 5-stage RL ladder circuit for the proposed strong-coupling analysis with those of 3-stage RL ladder circuit for the previous weak-coupling analysis.

The current I_n is calculated based on the play model in the proposed method (strong-coupling analysis) as shown in Eq. (4). In previous study (weak-coupling analysis), the second and third inductors (L_2 and L_3) have constant values and are given as fitting parameters. It is considered that our present method can perform accurate representations of hysteretic phenomena in comparison with those by methods in the previous study.

The fundamental frequency, modulation index, and switching dead time are set to 50 Hz, 0.7, and 3.5 μs, respectively, in our experiments and numerical simulations. The tests are performed at carrier frequencies of 1, 4, 12, and 20 kHz. The $I-V$ characteristics of semiconductors obtained from the catalog data sheet[27] are implemented in the numerical simulations based on previous method[18,21]. The DC voltage V_{dc} is adjusted to obtain the maximum magnetic flux density B_{max} of 1 T of the ring core. The fitting parameter α is obtained as 2.27 and the numerical iron loss is fitted to the measured one at f_{c} = 1 kHz. In previous study[21], L_2 (L_3) is also the fitting parameter and it is obtained as 5.6 (3.1) mH to equalize the numerical iron loss to the experimental one[21] at f_{c} = 1 kHz. See Refs.[18,20,21] for details of the previous weak-coupling analysis and parameter setting methods.

3 Results and discussion

Figure 2 shows the voltage waveforms induced in the magnetic core excited by the PWM inverter at f_{c} = 20 kHz. The previous study neglects the dead time. Our study considers the dead time of the inverter to evaluate its influence on the hysteresis curve. The voltage waveforms simulated by our present method with dead time agree well with the measured results. The previous results are not consistent with the experimental voltage because the dead time is neglected and the average height of V of the ON-mode that depends on V_{dc} differs from the experimental value in the previous method.

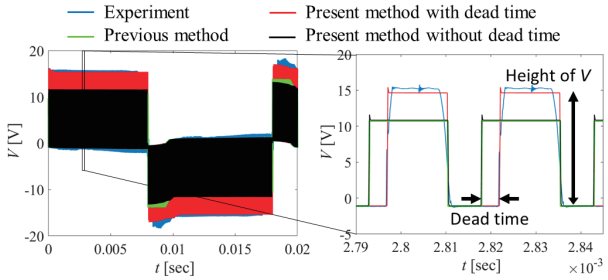

Fig. 2 Experimental and numerical waveforms of induced voltage V at f_c = 20 kHz and B_{max} = 1 T. Red and green curves are the results calculated using present (strong-coupling analysis) and previous (weak-coupling analysis[21]) methods, respectively. For comparison, blue and black lines show the results of experiments and present method without dead time. Magnified figure shows the influence of dead time.

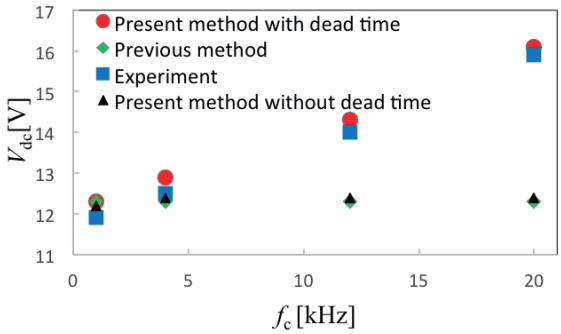

Fig. 3 Experimentally and numerically obtained DC voltage V_{dc} as a function of carrier frequency f_c at B_{max} = 1 T. For each test, V_{dc} is obtained at the maximum magnetic flux density B_{max} of 1 T. Tests are carried out at carrier frequencies f_c of 1, 4, 12, and 20 kHz.

Figure 3 shows the V_{dc} of the NO ring as a function of f_c at B_{max} = 1 T. The results obtained by the experiment and our numerical method (strong-coupling analysis) with dead time are in good agreement in terms of carrier frequency. However, the difference between the V_{dc} of the previous method[21] and the experimental values is extremely large, compared to present method with dead time, in the high carrier frequency region because the dead time is neglected as shown in the magnified portion in Fig. 2. The average errors of V_{dc} given by present and previous methods for the tested carrier frequency are about 2.5 % and 8.3 %, respectively. As shown in Figs. 2 and 3, we obtain accurate representations of the waveforms of V and V_{dc} because the dead time properties are considered.

We now discuss the magnetic hysteresis properties of the NO ring using strong-coupling analysis. Figure 4 plots the magnetic hysteresis curves for PWM waveform with a carrier frequency of 1, 4, 12, and 20 kHz. The experimental results are almost consistent with the numerical curves calculated by our present method with dead time. The experimental and numerical minor loops shown in the magnified figures differ (at f_c = 1 kHz). One

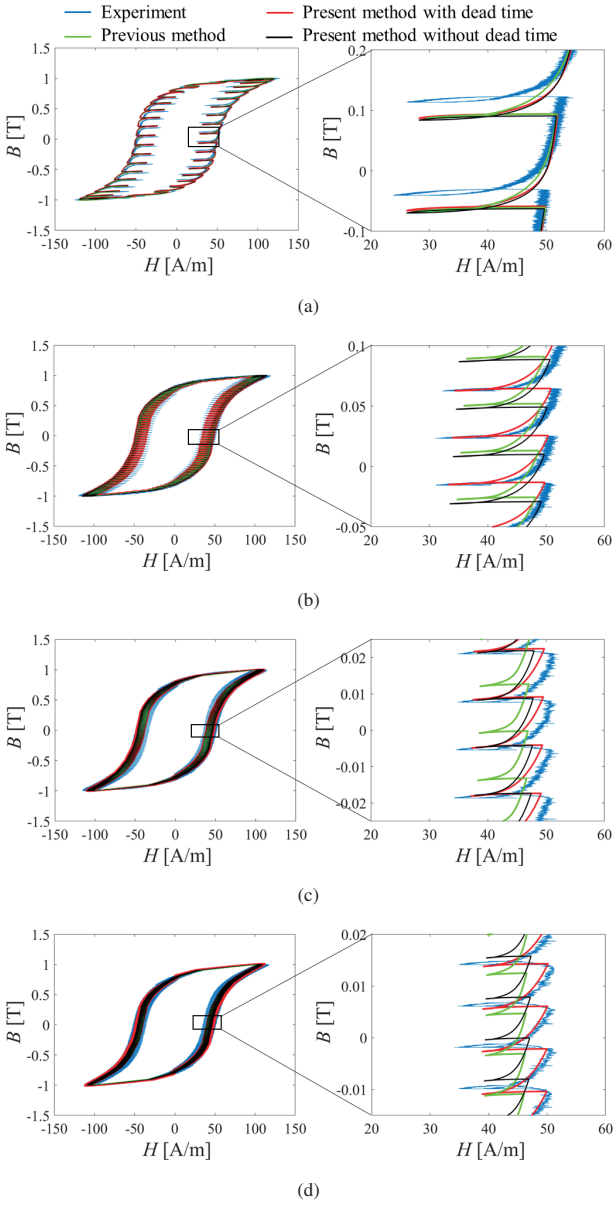

Fig. 4 Experimental and numerical hysteresis curves of NO ring under PWM inverter excitation. Magnified figures show minor loops of experimental and numerical hysteresis curves. (a) f_c = 1 kHz, (b) f_c = 4 kHz, (c) f_c = 12 kHz, and (d) f_c = 20 kHz.

of the reasons for this is that the $I - V$ property based on the catalog data sheet deviates from the experimental one. In the near future, the experimental $I - V$ properties of the semiconductors will be measured and then applied to numerical simulations. It is considered that the slight differences between experimental and numerical results calculated by our present method are caused by neglecting the rising and falling waveforms of voltage and current, frequency dependence of α, ringing noises, and so on, in the numerical simulations. In our future works, we will consider these phenomena in our strong-coupling analysis.

Figure 5 shows the W_{fe} as a function of f_c at B_{max} = 1 T. The average errors of iron losses calculated by strong- (present) and weak- (previous) coupling analysis are about 3 % and 6 %, re-

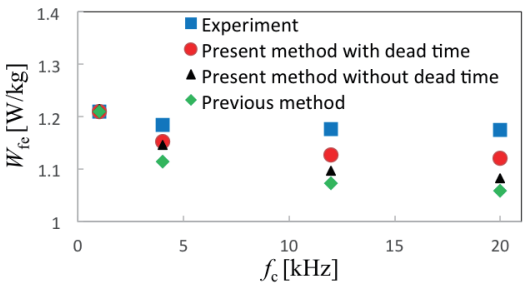

Fig. 5 Experimental and numerical iron loss W_{fe} as a function of carrier frequency f_c at B_{max} = 1 T.

spectively. Here, the average error is about 5 % when the strong-coupling analysis is used, and the effect of dead time is neglected (black points). We obtain accurate representations of hysteresis curves, especially in the high carrier frequency region, compared to those of the previous method because the dead time property is considered, the 5-stage *RL* ladder circuit is used, and the current I_n based on the play model is calculated in our present method (strong-coupling analysis). The proposed strong-coupling analysis obtains accurate iron losses and hysteresis curves under PWM inverter excitation in comparison with previous study.

4 Conclusion

This paper addressed the numerical expression for magnetic hysteresis properties under PWM inverter excitation using the strong-coupling analysis of electricity and magnetism. The dynamic hysteresis model (the play model with the Cauer circuit) was implemented in the circuit simulator to realize the strong-coupling analysis. We showed that, by accounting for dead time properties, the numerical voltage waveforms calculated by the strong-coupling analysis were consistent with the experimental results, whereas the results calculated by previous method were not. It was also shown that the hysteresis curves simulated by our strong-coupling analysis agreed well with the measured results in comparison with the results of previous study because the dead time property was considered, the 5-stage *RL* ladder circuit was used, and the current I_n based on the play model was calculated.

Acknowledgment This work was partly supported by the JSPS KAKENHI ♯18K13749, JST OPERA ♯JPMJOP1841, JFE 21st Century Foundation, Kansai Research Foundation, Takeuchi Foundation, and Nagamori Foundation Research Grant. We are grateful to Prof. T. Matsuo (Kyoto University) for his support to make programs.

References

1) A. Boglietti, P. Ferraris, M. Lazzari, and M. Pastorelli: *IEEE Trans. Magn.*, **32**, 4884 (1996).
2) A. Boglietti, P. Ferraris, M. Lazzari, and F. Profumo: *IEEE Trans. Magn.*, **27**, 5334 (1991).
3) A. Boglietti, P. Ferraris, M. Lazzari, and M. Pastorelli: *IEEE Trans. Magn.*, **31**, 4250 (1995).
4) M. Kawabe, T. Nomiyama, A. Shiozaki, H. Kaihara, N. Takahashi, and M. Nakano: *IEEE Trans. Magn.*, **48**, 3458 (2012).
5) K. Fujisaki and S. Liu: *J. Appl. Phys.*, **115**, 17A321, (2014).
6) S. Odawara, K. Fujisaki, and F. Ikeda: *IEEE Trans. Magn.*, **50**, 11-1 (2014).
7) T. Taitoda, Y. Takahashi, and K. Fujiwara: *IEEE Trans. Magn.*, **51**, 11-1 (2015).
8) A. Yao, K. Tsukada, S. Odawara, K. Fujisaki, Y. Shindo, N. Yoshikawa, and T. Yoshitake: *AIP Adv.*, **7**, 056618, (2017).
9) A. Yao and K. Fujisaki: Proc. LDIA 2017, Osaka, 2017, p. 1 (IEEE, 2017).
10) A. Yao, T. Sugimoto, S. Odawara, and K. Fujisaki: *AIP Adv.*, **8**, 056804, (2018).
11) A. Yao, T. Sugimoto, S. Odawara, and K. Fujisaki: *IEEE Trans. Magn.*, **54**, 11-1 (2018).
12) S. Bobbio, G. Milano, C. Serpico, and C. Visone: *IEEE Trans. Magn.*, **33**, 4417 (1997).
13) T. Matsuo and M. Shimasaki: *IEEE Trans. Magn.*, **41**, 3112 (2005).
14) J. Kitao, K. Hashimoto, Y. Takahashi, K. Fujiwara, Y. Ishihara, A. Ahagon, and T. Matsuo: *IEEE Trans. Magn.*, **48**, 3375 (2012).
15) J. H. Krah: *IEEE Trans. Magn.*, **41**, 1444 (2005).
16) Y. Shindo and O. Noro: *IEEJ Trans. Fund. Mater.*, **134**, 173 (2014).
17) Y. Shindo, T. Miyazaki, and T. Matsuo: *IEEE Trans. Magn.*, **52**, 3-1 (2016).
18) S. Odawara, K. Fujisaki, T. Matsuo, and Y. Shindo: *IEEJ J. Ind. Appl.*, **135**, 1191 (2015).
19) T. Miyazaki, T. Mifune, T. Matsuo, Y. Shindo, Y. Takahashi, and K. Fujiwara: *J. Appl. Phys.*, **117**, 17D110, (2015).
20) A. Yao, S. Odawara, and K. Fujisaki: *IEEJ J. Ind. Appl.*, **7**, 298 (2018).
21) S. Odawara and K. Fujisaki: *IEEE Trans. Magn.*, **54**, 5-1 (2018).
22) A. Yao and T. Hatakeyama: *J. Magn. Soc. Jpn.*, **43**, 46 (2019).
23) A. Yao, K. Tsukada, and K. Fujisaki: Proc. LDIA 2017, Osaka, 2017, p. 1 (IEEE, 2017).
24) A. Yao, K. Tsukada, and K. Fujisaki: *IEEJ J. Ind. Appl.*, **7**, 321 (2018).
25) Y. Tanaka, S. Koga, R. Kogi, S. Odawara, and K. Fujisaki: *IEEJ J. Ind. Appl.*, **136**, 110 (2016).
26) Y. Shindo: *IEEJ Journal*, **137**, 534 (2017).
27) *Catalog PM75RSD060 (in Japanese)*. Mitsubishi Electric Corporation.

Recieved Aug. 7, 2019; Accepted Sep. 20, 2019

J. Magn. Soc. Jpn., **43**, 109-113 (2019)

<Paper>

Influence of Cap-Layer on the Structure of FePt Alloy Thin Film Formed on VN and VC Underlayers

Tomoki Shimizu[1,2], Mitsuru Ohtake[1], Masaaki Futamoto[2], Fumiyoshi Kirino[3], and Nobuyuki Inaba[4]

[1]Faculty of Engineering, Yokohama National University, *79-5 Tokiwadai, Hodagaya, Yokohama 240-8501, Japan*
[2]Faculty of Science and Engineering, Chuo University, *1-13-27 Kasuga, Bunkyo-ku, Tokyo 112-8551, Japan*
[3]Graduate School of Fine Arts, Tokyo University of the Arts, *12-8 Ueno-koen, Taito-ku, Tokyo 110-8714, Japan*
[4]Faculty of Engineering, Yamagata University, *4-3-16 Jyonan, Yonezawa, Yamagata 992-8510, Japan*

10-nm-thick FePt alloy films without and with MgO, VC, and VN cap-layers of 2 nm thickness are prepared on MgO, VC, and VN single-crystal underlayers of (001) orientation by using a two-step method consisting of low-temperature deposition at 200 °C followed by high-temperature annealing at 600 °C. The surface energies of MgO and vanadium compounds (VC, VN) are respectively lower and higher than that of FePt alloy. The influences of combination of underlayer and cap-layer materials on the surface flatness, the lattice deformation, the degree of $L1_0$ ordering, and the magnetic anisotropy are investigated. FePt(001) single-crystal films without and with MgO, VC, and VN(001) single-crystal cap-layers grow epitaxially on all the underlayers. The in-plane lattice of FePt film is expanded in accommodation of lattice mismatch with underlayer and/or cap-layer. The lattice deformation aligns the *c*-axis perpendicular to the substrate surface and enhances $L1_0$ ordering. A higher order degree and a stronger perpendicular magnetic anisotropy are obtained by using a combination of VN underlayer and MgO cap-layer. The present study shows that employment of underlayer and cap-layer materials whose surface energies are respectively higher and lower than that of FePt alloy is effective in enhancing order degree and magnetic anisotropy.

Key words: $L1_0$ ordered FePt film, surface energy, underlayer, cap-layer, perpendicular magnetic anisotropy

1. Introduction

FePt alloy with $L1_0$ structure shows a uniaxial magnetocrystalline anisotropy energy greater than 10^7 erg/cm^3 along the *c*-axis[1] and the thin films have been investigated for applications to energy-assisted magnetic recording media, magnetoresistive random access memory devices, etc. For such applications, it is important to prepare an FePt film with flat surface, high order degree, and *c*-axis normal to the substrate.

FePt films have been frequently prepared on (001)-oriented MgO underlayers or substrates[2–11]. The lattice constant of MgO crystal (a = 0.4212 nm[12]) is larger than that of $L1_0$-FePt crystal (a = 0.3842 nm, c = 0.3702 nm[13]). Thus when FePt films grow epitaxially on MgO underlayers or substrates, the FePt lattice is expanded along the in-plane direction in accommodation of the lattice mismatch of $[(a_{FePt} - a_{MgO}) / a_{MgO}] \times 100 = -8.8\%$ at the FePt/MgO interface and the *c*-axis is expected to be preferentially oriented along the perpendicular direction.

When growth of an upper layer on a lower layer follows Volmer-Weber (island-like growth) mode, the upper layer consists of isolated islands and involves surface undulations. The contact angle of island of upper layer with respect to the lower layer is expressed by the Young's relation where the contact angle depends on the combination of surface energies of upper and lower layer materials. In order to improve the surface flatness and further enhance the in-plane tensile stress caused by lattice mismatch, it seems useful to employ underlayer and cap-layer materials whose surface energies are respectively larger and lower than that of FePt alloy (2.1 J/m^2)[14].

Vanadium nitride (VN) and vanadium carbide (VC) crystals have $B1$ (NaCl-type) structure, which is same with that of MgO crystal. The lattice constants of MgO, VC, and VN crystals are respectively 0.4212, 0.4165, and 0.4135 nm and the difference is less than 2%. On the other hand, the surface energies of VN (2.7 J/m^2)[15] and VC (2.8 J/m^2)[16] crystals are much larger than that of MgO (1.5 J/m^2)[17] crystal. Thus, combination of VN or VC underlayer and MgO cap-layer seems to be effective.

In our previous studies[18,19], FePt films of 10 nm thickness without cap-layers were prepared on MgO, VN, and VC(001) single-crystal underlayers by using two different methods. One was a one-step method consisting of high-temperature deposition at 600 °C. The other was a two-step method composed of low-temperature deposition at 200 °C followed by the high-temperature annealing at 600 °C. When the one-step method was used, the FePt film formed on MgO(001) underlayer possessed an island-like surface, whereas flat surface was observed for the films formed on VN and VC underlayers. On the contrary, flat surface was realized for the films prepared on all the underlayers by using the two-step method, since the low-temperature deposition suppressed the surface migration and the clustering of deposited atoms.

In the present study, three kinds of cap-layer, MgO, VN, and VC, are applied to the FePt films prepared on MgO, VN, and VC(001) single-crystal underlayers by employing the two-step method. The effects of underlayer/cap-layer combination on the surface flatness, the lattice parameter, the degree of $L1_0$ ordering, and the magnetic anisotropy are investigated.

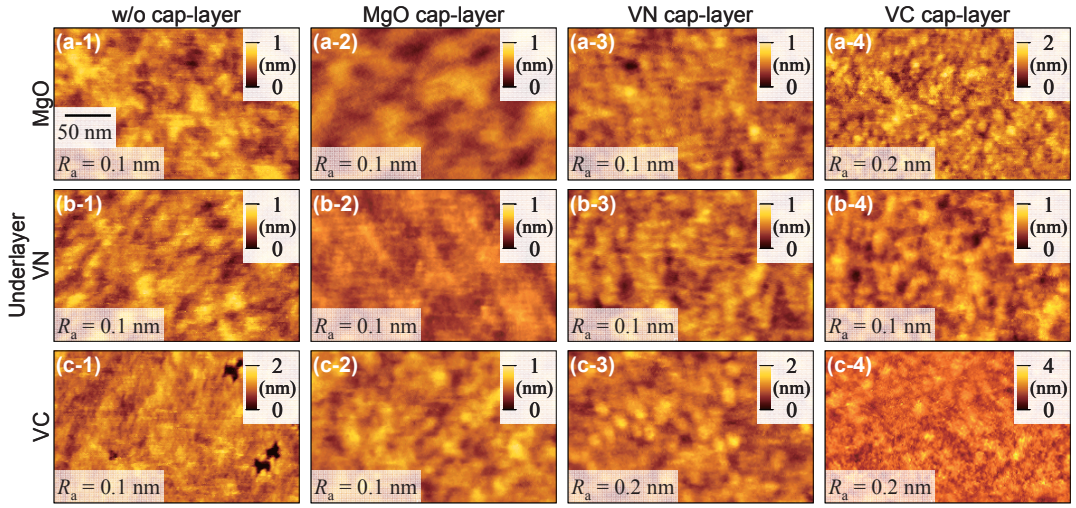

Fig. 1 AFM images observed for FePt films prepared on (a) MgO, (b) VN, and (c) VC underlayers (a-1)–(c-1) without and with (a-2)–(c-2) MgO, (a-3)–(c-3) VN, and (a-4)–(c-4) VC cap-layers.

2. Experimental Procedure

Thin films were prepared on (001) single-crystal substrates of $SrTiO_3$ (a = 0.3905 nm[20]) by using a radio-frequency (RF) magnetron sputtering system equipped with a reflection high-energy electron diffraction (RHEED) facility. The base pressures were lower than 4×10^{-7} Pa. $Fe_{50}Pt_{50}$ (at. %) alloy, MgO, VN, and VC targets of 3 inch diameter were employed and the respective RF powers were set at 43, 200, 96, and 95 W. The distance between target and substrate and the Ar gas pressure were fixed at 150 mm and 0.67 Pa, respectively. Under these conditions, the deposition rate was 0.015 nm/s for MgO, whereas it was 0.020 nm/s for the other materials.

Before deposition, $SrTiO_3$(001) substrates were heated at 600 °C for 1 hour to obtain clean surfaces. 2-nm-thick MgO, VN, and VC single-crystal underlayers of (001) orientation were prepared through epitaxial growth on the substrates at 600 °C. 10-nm-thick FePt films and 2-nm-thick cap-layers of MgO, VN, or VC were sequentially formed on the single-crystal underlayers at a substrate temperature of 200 °C. Then, these samples were annealed at 600 °C (two-step method).

The crystallographic structure and orientation were studied by RHEED. The structural properties were investigated by $2\theta/\omega$-scan out-of-plane and $2\chi/\varphi$-scan in-plane X-ray diffractions (XRDs) with Cu-Kα radiation (λ = 0.15418 nm). The surface morphology was observed by atomic force microscopy (AFM). The magnetization curves were measured by vibrating sample magnetometry.

3. Results and Discussion

Figure 1 shows the AFM images observed for FePt films without and with MgO, VN, and VC cap-layers on MgO, VN, and VC(001) single-crystal underlayers prepared by two-step method. The FePt films both without and with cap-layers have flat surfaces with the arithmetical mean surface roughness (R_a) values of 0.1–0.2 nm. The two-step method prevents the surface migration and the clustering of deposited atoms, similar to our previous study[19].

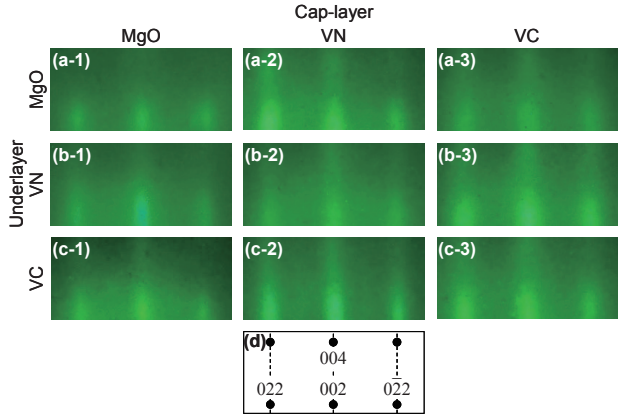

Fig. 2 (a)–(c) RHEED patterns observed for FePt films with (a-1)–(c-1) MgO, (a-2)–(c-2) VN, and (a-3)–(c-3) VC cap-layers prepared on (a) MgO, (b) VN, and (c) VC underlayers. (d) Schematic diagram of diffraction pattern simulated for $B1$(001) single-crystal surface. The incident electron beam is parallel to [100].

Figures 2(a)–(c) show the RHEED patterns observed for MgO, VN, and VC cap-layers formed on FePt films. Streaks are recognized for all the cap-layers, suggesting that the cap-layers are epitaxially grown on FePt films. Figure 2(d) shows the schematic diagram of diffraction patterns simulated for a $B1$(001) single-crystal surface. The observed patterns seem to agree with the simulated pattern. The crystallographic orientation relationships are determined as follows,

MgO, VN, VC(001)[100]$_{\text{cap-layer}}$
|| $L1_0$-FePt(001)[100]
|| MgO, VN, VC(001)[100]$_{\text{underlayer}}$
|| $SrTiO_3$(001)[100]$_{\text{substrate}}$.

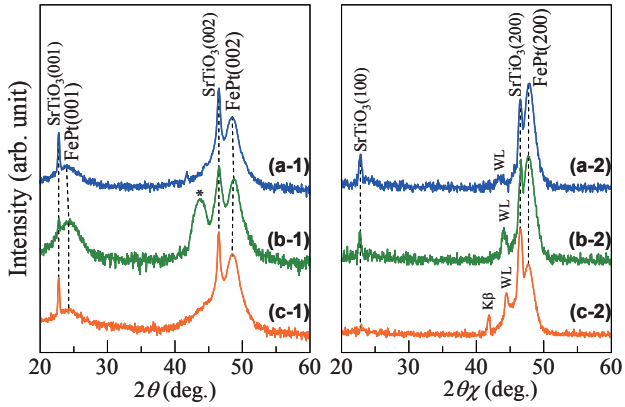

Fig. 3 (a-1)–(c-1) Out-of-plane and (a-2)–(c-2) in-plane XRD patterns observed for FePt films without cap-layers prepared on (a) MgO, (b) VN, and (c) VC underlayers. The reflection shown by * is not identified. The intensity is shown in logarithmic scale.

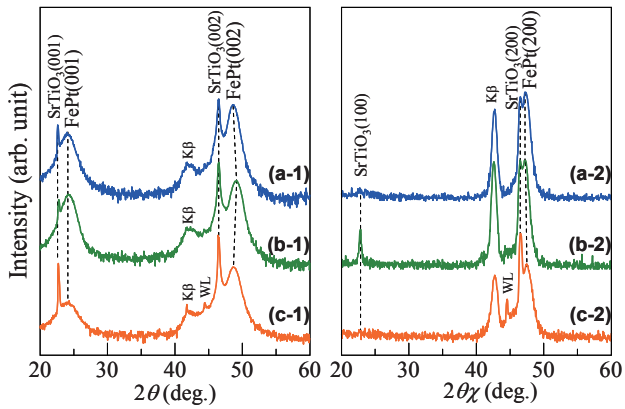

Fig. 4 (a-1)–(c-1) Out-of-plane and (a-2)–(c-2) in-plane XRD patterns observed for FePt films with MgO cap-layers prepared on (a) MgO, (b) VN, and (c) VC underlayers. The intensity is shown in logarithmic scale.

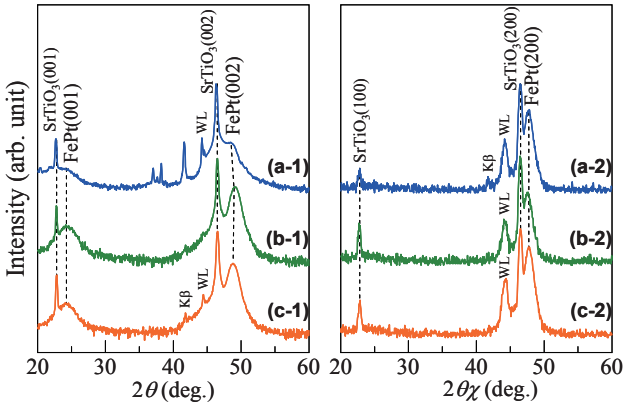

Fig. 5 (a-1)–(c-1) Out-of-plane and (a-2)–(c-2) in-plane XRD patterns observed for FePt films with VN cap-layers prepared on (a) MgO, (b) VN, and (c) VC underlayers. The intensity is shown in logarithmic scale.

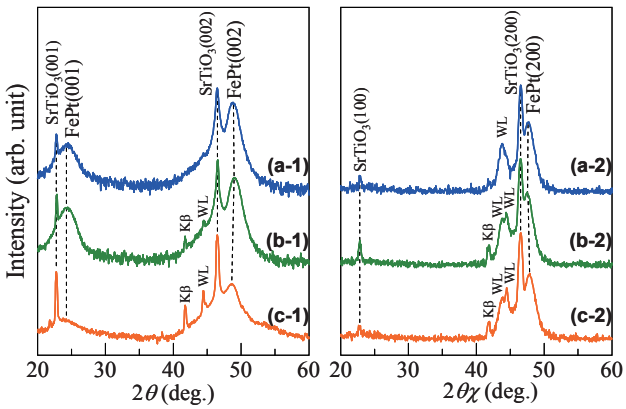

Fig. 6 (a-1)–(c-1) Out-of-plane and (a-2)–(c-2) in-plane XRD patterns observed for FePt with VC cap-layers films prepared on (a) MgO, (b) VN, and (c) VC underlayers. The intensity is shown in logarithmic scale.

Figures 3–6 show the out-of-plane and in-plane XRD patterns measured for the FePt films without and with cap-layers prepared on MgO, VN, and VC underlayers. For all the films, fundamental reflections of FePt(002) and (200) are clearly observed in the out-of-plane and in-plane patterns, respectively. On the contrary, superlattice reflection of FePt(001) are recognized only in the out-of-plane patterns. The results show that the FePt films consist of $L1_0$(001) crystal with the *c*-axis normal to the substrate surface and do not involve $L1_0$(100) and (010) crystals whose *c*-axes are lying in the film plane.

Figures 7(a) and (b) show the in-plane and the out-of-plane lattice constants, *a* and *c*, calculated from the peak angles of FePt(200) and FePt(002) reflections, respectively. The *a* value is larger than the *c* value for the respective films. Figure 7(c) summarizes the ratios of out-of-plane to in-plane lattice constants, *c*/*a*. The *c*/*a* ratio decreases by employing VN underlayer and MgO cap-layer as shown in Figs. 7(c-1) and (c-2), respectively. Figure 7(d) shows the order degrees, *S*, which are calculated by comparing the intensities of FePt(001) superlattice and (002) fundamental reflections. The $L1_0$ ordering is enhanced by using VN underlayer and MgO cap-layer as shown in Figs. 7(d-1) and (d-2), respectively. A higher *S* values is corresponding to a lower *c*/*a* ratio. These results show that employment of underlayer and cap-layer whose surface energies are respectively larger (VN) and smaller (MgO) than that of FePt alloy is effective for enhancing in-plane tensile stress and $L1_0$ ordering.

Figure 8 shows the magnetization curves measured for FePt films without and with MgO cap-layer formed on MgO and VN underlayers. The difference of *M*-*H* curves measured in longitudinal and perpendicular directions is small for the films without cap-layer [Figs. 8(a-1), (b-1)]. The reason is due to that the *S* value is lower than 0.2. On the contrary, strong perpendicular magnetic anisotropies are clearly observed for the FePt films with cap-layers, where the *S* value is higher than 0.5. The out-of-plane coercivities of films with MgO cap-layers formed on MgO and VN underlayers are as

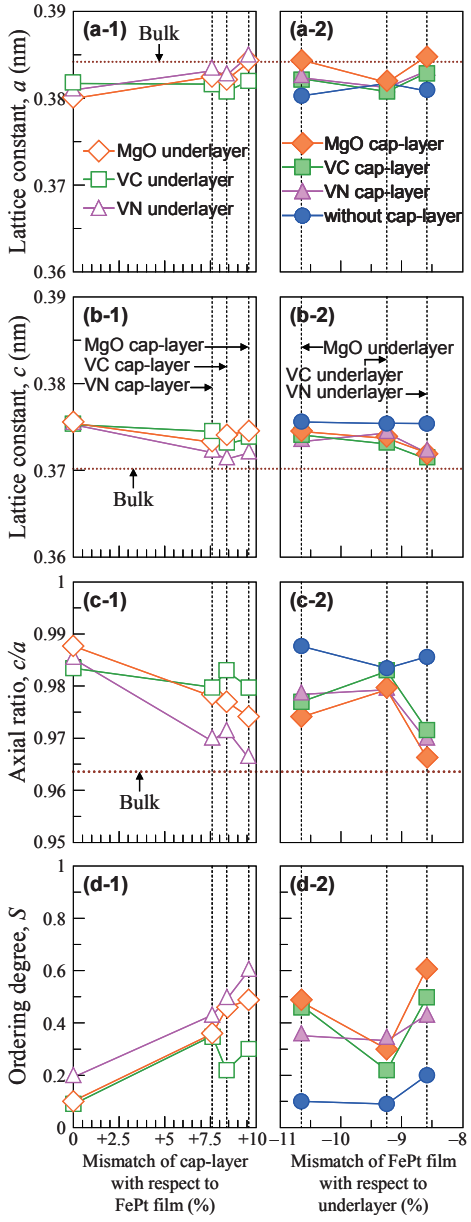

Fig. 7 Dependences of (a-1)–(d-1) underlayer and (a-2)–(d-2) cap-layer materials on the lattice parameters of (a) *a*, (b) *c*, (c) *c*/*a*, and (d) the order degree, *S*.

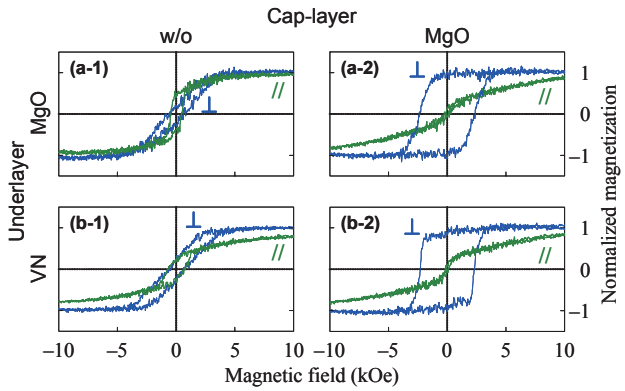

Fig. 8 Magnetization curves measured for FePt films (a-1, b-1) without and (a-2, b-2) with MgO cap-layers prepared on (a) MgO and (b) VN underlayers.

small as 2.4 and 2.3 kOe, respectively. The magnetization seems to reverse by domain wall motion, because the films have continuous structure with flat surfaces. The FePt film with MgO cap-layer formed on VN underlayer shows a slightly stronger perpendicular anisotropy than that with MgO cap-layer formed on MgO underlayer. The combination of VN underlayer and MgO cap-layer is giving the highest order degree and magnetic anisotropy.

4. Conclusion

FePt thin films without and with MgO, VC, and VN cap-layers are prepared on MgO, VC, and VN single-crystal underlayers of (001) orientation. The effects of combination of underlayer and cap-layer materials on the structural and magnetic properties are investigated. FePt(001) single-crystal films without and with MgO, VC, and VN(001) single-crystal cap-layers are obtained on all the underlayers. The FePt lattice is expanded along the in-plane direction due to accommodation of lattice misfit with underlayer and/or cap-layer. The lattice strain aligns the *c*-axis normal to the substrate surface and enhances $L1_0$ ordering. A higher order degree and a stronger perpendicular magnetic anisotropy are obtained by employing a combination of VN underlayer and MgO cap-layer. Introduction of underlayer and cap-layer materials whose surface energies are respectively higher and lower than that of FePt alloy is effective in enhancing order degree and perpendicular magnetic anisotropy.

References

1) O. A. Ivanov, L. V. Solina, V. A. Demshina, and L. M. Magat: *Fiz. Metal Metalloved.*, **35**, 81 (1973).
2) B. M. Lairson, M. R. Visokay, R. Sinclair, and B. M. Clemens: *Appl. Phys. Lett.*, **62**, 639 (1993).
3) A. Cebollada, D. Weller, J. Sticht, G. R. Harp, R. F. C. Farrow, R. F. Marks, R. Savoy, and J. C. Scott: *Phys. Rev. B*, **50**, 3419 (1994).
4) S. Okamoto, N. Kikuchi, O. Kitakami, T. Miyazaki, Y. Shimada, and K. Fukamichi: *Phys. Rev. B*, **66**, 024413 (2002).
5) T. Shima, K. Takanashi, Y. K. Takahashi, and K. Hono: *Appl. Phys. Lett.*, **81**, 1050 (2002).
6) M. Weisheit, L. Schultz, and S. Fähler: *J. Appl. Phys.*, **95**, 7489 (2004).
7) R. Ikeda, M. Kagami, T. Kato, S. Iwata, and S. Tsunashima: *J. Magn. Soc. Jpn.*, **33**, 493 (2009).
8) M. Ohtake, S. Ouchi, F. Kirino, and M. Futamoto: *J. Appl. Phys.*, **111**, 07A708 (2012).
9) H. Ho, J. Zhu, A. Kulovits, D. E. Laughlin, and J. G. Zhu: *J. Appl. Phys.*, **116**, 193510 (2014).
10) M. Ohtake, A. Itabashi, M. Futamoto, F. Kirino, and N. Inaba: *IEEE Trans. Magn.*, **50**, 2104204 (2014).
11) M. Ohtake, Akira Itabashi, M. Futamoto, F. Kirino, and N. Inaba: *J. Magn. Soc. Jpn.*, **39**, 167 (2015).
12) P. Karen, A. Kjekshus, Q. Huang, and V. L. Karen: *J. Alloy Compd.*, **282**, 72 (1998).
13) A. Menshikov, T. Tarnocazi, and E. Kren: *Phys. Status Solidi A*, **28**, K85 (1975).
14) A. Dannenberg, M. E. Gruner, A. Hucht, and P. Entel: *Phys. Rev. B*, **80**, 245438 (2009).
15) R. Nakanishi, S. Kunitsugu, and K. Sueoka: *J. Surf.*

Finish. Soc. Jpn., **61**, 535 (2010).
16) H. W. Hugosson, O. Eriksson, U. Jasson, A. V. Ruban, P. Souvatzis, and I. A. Abrikosov: *Sur. Sci.*, **557**, 243 (2004).
17) R. A. Evarestov and A. V. Bandura: *Inter. J. Quantum Chem.*, **100**, 452 (2004).
18) T. Shimizu, M. Nakamura, R. Ochiai, M. Ohtake, M. Futamoto, F. Kirino, and N. Inaba: *IEICE Tech. Rep.*, **MR2016-40**, 63 (2016).
19) T. Shimizu, M. Ohtake, M. Futamoto, F. Kirino, and N. Inaba: *IEEE Trans. Magn.*, **53**, 2101904 (2017).
20) F. W. Lytle: *J. Appl. Phys.*, **35**, 2212 (2004).

Received Oct. 17, 2017; Revised Jun. 24, 2019; Accepted Aug. 9, 2019

J. Magn. Soc. Jpn., **43**, 114-119 (2019)

<Paper>

Information Stability in Heat-Assisted Magnetic Recording

T. Kobayashi, Y. Nakatani*, and Y. Fujiwara

Graduate School of Engineering, Mie Univ., *1577 Kurimamachiya-cho, Tsu 514-8507, Japan*

*Graduate School of Informatics and Engineering, Univ. of Electro-Communications, *1-5-1 Chofugaoka, Chofu 182-8585, Japan*

The thermal stability factor $K_{um}V_m/kT$ and the anisotropy constant ratio K_u/K_{bulk} necessary for 10 years of archiving in heat-assisted magnetic recording of 2 Tbpsi are evaluated by employing a bit error rate calculation using a grain error probability P. Although the attempt frequency f_0 in P is a function of the Gilbert damping constant, the Curie temperature, K_u/K_{bulk}, the grain volume, and temperature, f_0 can be treated as a constant. The Gilbert damping constant and the Curie temperature variation are parameters with little impact. On the other hand, the grain size variation, the grain number per bit n, the mean Curie temperature T_{cm}, and the storage temperature T are parameters with a strong impact on bit error rate. Although $K_{um}V_m/kT$ decreases as n increases due to a statistical problem, a larger K_u/K_{bulk} is necessary as n increases due to a smaller grain size. A larger K_u/K_{bulk} is also necessary as T_{cm} decreases. The bit error rate increases rapidly as T increases.

Key words: thermal stability factor, anisotropy constant ratio, bit error rate, probability, attempt frequency

1. Introduction

The long-term stability of archived information is one of the most important properties of magnetic recording media. This stability has been widely discussed using the thermal stability factor $K_{um}V_m/kT$, where K_{um}, V_m, k, and T are the mean grain anisotropy constant, the grain volume for the mean grain size of the medium, the Boltzmann constant, and temperature, respectively[1]. We have already estimated the numerical value of $K_{um}V_m/kT$ by employing a bit error rate calculation using the grain error probability for various grain numbers per bit n and the standard deviations of grain size σ_D[2),3)]. In that calculation, we used a constant attempt frequency f_0 of 1.0×10^{11} s^{-1}. However, precisely speaking, f_0 is a function of the Gilbert damping constant α, the magnetization M_s, the anisotropy field H_k, the grain volume V, and T[4)].

Heat-assisted magnetic recording (HAMR) is a promising candidate as a next generation magnetic recording method that can operate beyond the trilemma limit[1]. HAMR is a recording method in which the medium is heated to reduce coercivity during the writing period. We have introduced a HAMR design parameter, namely, the medium anisotropy constant ratio K_u/K_{bulk}[5)] in place of the medium anisotropy constant K_u since the K_u value at the storage temperature is a function of the medium Curie temperature T_c, which is strongly related to the writing property. K_u/K_{bulk} is the intrinsic ratio of the medium K_u to bulk FePt K_u regardless of T_c where FePt is a candidate HAMR medium material thanks to its large K_u and a relatively low T_c. A medium with a high K_u/K_{bulk}, *e.g.* 0.6 - 1.0[6)], is difficult to manufacture regardless of T_c. M_s is a function of T_c and T. $H_k = 2K_u/M_s$ is a function of T_c, K_u/K_{bulk}, and T. And V_m is a function of n under a constant grain height. Therefore, f_0 is a function of α, T_c, T, K_u/K_{bulk}, and n.

In this paper, we evaluate the $K_{um}V_m/kT$ and K_u/K_{bulk} necessary for 10 years of archiving in 2 Tbpsi HAMR by employing a bit error rate calculation using the grain error probability, which includes f_0 as a function of α, T_c, T, K_u/K_{bulk}, and n. Furthermore, we also examine the dependence of the bit error rate on the standard deviation of the Curie temperature as well as that of the grain size.

2. Calculation Method

2.1 Attempt frequency

The thermal stability factor $K_{um}V_m/kT$ and the anisotropy constant ratio K_u/K_{bulk} necessary for 10 years of archiving in 2 Tbpsi HAMR were evaluated by employing a bit error rate calculation using the grain error probability P

$$P = 1 - \exp\left(-f_0 t \exp\left(-\frac{K_u V_m}{kT}\cdot\left(\frac{D}{D_m}\right)^2\right)\right) \quad (1)$$

where f_0, t, K_u, V_m, k, T, and D are the attempt frequency, time, the grain anisotropy constant, the grain volume for mean grain size D_m, the Boltzmann constant, temperature, and the grain size, respectively.

The attempt frequency f_0 has been deduced as

$$f_0 = \frac{\alpha\gamma}{1+\alpha^2}\sqrt{\frac{M_s H_k^3 V}{2\pi kT}}\left(1-\left(\frac{H}{H_k}\right)^2\right)\left(1+\frac{H}{H_k}\right) \quad (2)$$

under a magnetic field H where α, γ, M_s, H_k, and V are the Gilbert damping constant, the gyromagnetic ratio, the magnetization, the anisotropy field $H_k = 2K_u/M_s$, and the grain volume, respectively[4)]. M_s and H change from parallel to antiparallel for $H > 0$, and antiparallel to parallel for $H < 0$.

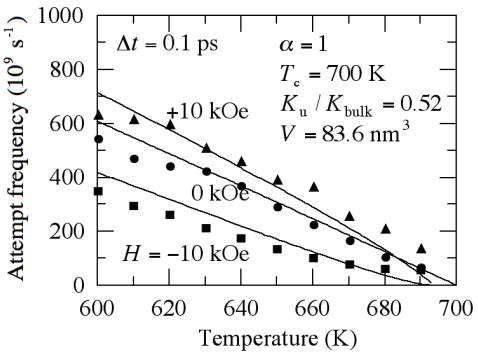

Fig. 1 Temperature dependence of attempt frequency for various magnetic fields H.

Figure 1 shows the temperature dependence of f_0 for various H values under the conditions where α = 1, the Curie temperature T_c = 700 K, K_u / K_{bulk} = 0.52, and V = 83.6 nm^3.

The solid lines were calculated using Eq. (2). The temperature dependence of M_s was determined by employing a mean field analysis[7], and that of K_u was assumed to be proportional to M_s^2[8]. The T_c value was adjusted by the Cu simple dilution of $(Fe_{0.5}Pt_{0.5})_{1-z}Cu_z$. $M_s(T_c, T)$ is a function of T_c and T, and $M_s(T_c = 770\ \mathrm{K}, T = 300\ \mathrm{K})$ = 1000 emu/cm^3 was assumed for FePt (Cu composition z = 0). $K_u(T_c, K_u / K_{bulk}, T)$ is a function of T_c, K_u / K_{bulk}, and T where

$$K_u / K_{bulk} = \frac{K_u(T_c, K_u / K_{bulk}, T)}{K_u(T_c, K_u / K_{bulk} = 1, T)}. \quad (3)$$

$K_u(T_c = 770\ \mathrm{K}, K_u / K_{bulk} = 1, T = 300\ \mathrm{K})$ = 70 Merg/cm^3 was assumed for FePt (z = 0). We used $M_s(T_c = 700\ \mathrm{K}, T)$ and $K_u(T_c = 700\ \mathrm{K}, K_u / K_{bulk} = 0.52, T)$ in Fig. 1.

The filled symbols were obtained with a conventional micromagnetic calculation using the Landau-Lifshitz-Gilbert equation[9]. The calculation step time Δt was 0.1 ps. Usually Landau-Lifshitz-Bloch (LLB) equation is used for the simulation near Curie temperature[10]. However we used the Langevin equation with the effect of the temperature on the material parameters, which is the biggest different point between the LLB and the Langevin equation. Therefore the effect of the equation on the simulation is permissible.

Although we discuss the information stability around room temperature in this paper, the comparison was carried out for high temperature region since room temperature is too low to calculate in a short time when employing the micromagnetic calculation. Since the results represented by the solid lines and the filled symbols agree well, the attempt frequency was calculated using Eq. (2) in this paper.

Neither the demagnetizing nor the magnetostatic fields were considered in this paper for simplifying the model calculation. The problem of these fields is a future subject.

2.2 Bit error rate calculation

The bit error rate was calculated using each grain error probability P_i of Eq. (1). For example, for 4 grains/bit, the 1 grain-error bit error rate ${}_4\mathrm{bER}_1$ is expressed as

$${}_4\mathrm{bER}_1 = Er_1P_1(1-P_2)(1-P_3)(1-P_4) + \cdots + Er_4(1-P_1)(1-P_2)(1-P_3)P_4, \quad (4)$$

the 2 grain-error bit error rate ${}_4\mathrm{bER}_2$

$${}_4\mathrm{bER}_2 = Er_{12}P_1P_2(1-P_3)(1-P_4) + \cdots + Er_{34}(1-P_1)(1-P_2)P_3P_4, \quad (5)$$

the 3 grain-error bit error rate ${}_4\mathrm{bER}_3$

$${}_4\mathrm{bER}_3 = Er_{123}P_1P_2P_3(1-P_4) + \cdots + Er_{234}(1-P_1)P_2P_3P_4, \quad (6)$$

and the 4 grain-error bit error rate ${}_4\mathrm{bER}_4$

$${}_4\mathrm{bER}_4 = P_1P_2P_3P_4 \quad (7)$$

where

$$Er_j = 1, \text{ if } \frac{\sum_i M_{si}(T_{ci}, T)D_i^2}{n \cdot M_s(T_{cm}, T)D_m^2} < 0.5, \quad (8)$$

and

$$Er_j = 0, \text{ if } \frac{\sum_i M_{si}(T_{ci}, T)D_i^2}{n \cdot M_s(T_{cm}, T)D_m^2} \geq 0.5. \quad (9)$$

Errors occur in some grains of a bit. We assume that if the surface magnetic charge of the grains where the magnetization turns in the recording direction $\sum M_{si}(T_{ci}, T)D_i^2$ is more than 50 % (signal threshold) of the total surface magnetic charge in a bit $n \cdot M_s(T_{cm}, T)D_m^2$, the bit is error free where M_{si}, T_{ci}, D_i, n, T_{cm}, and D_m are the magnetization, the Curie temperature, the grain size of the i-th grain, the grain number per bit, the mean Curie temperature, and the mean grain size, respectively.

After all, the total bit error rate ${}_4\mathrm{bER}$ is the summation of each bit error rate ${}_4\mathrm{bER}_k$ as follows

$${}_4\mathrm{bER} = \sum_k {}_4\mathrm{bER}_k. \quad (10)$$

The bit error rate is a function of the anisotropy constant ratio K_u / K_{bulk}. Therefore, we obtained K_u / K_{bulk} for a certain bit error rate. Since the mean anisotropy constant K_{um} is a function of K_u / K_{bulk}, the thermal stability factor $K_{um}V_m / kT$ was calculated using K_u / K_{bulk}.

3. Calculation Results

3.1 Information stability for 10 years of archiving

The calculation conditions are summarized in Table 1. The recording density is 2 Tbpsi, and the area S of a bit is 323 nm^2. The medium was assumed to be

granular in which each bit has n grains/bit. The mean grain size D_m was determined by

$$D_m = \sqrt{\frac{S}{n}} - \Delta \qquad (11)$$

where the non-magnetic spacing Δ was assumed to be 1 nm. The grain height h was 8 nm, and so the grain volume V_m for D_m was $D_m \times D_m \times h$.

Table 1 Calculation conditions for 10 years of archiving.

Recording density (Tbpsi)	2
Non-magnetic spacing Δ (nm)	1
Grain height h (nm)	8
Storage temperature T (K)	300
Storage time t (years)	10
Signal threshold	0.5
Bit number (bits)	10^7
Bit error rate	1E-3

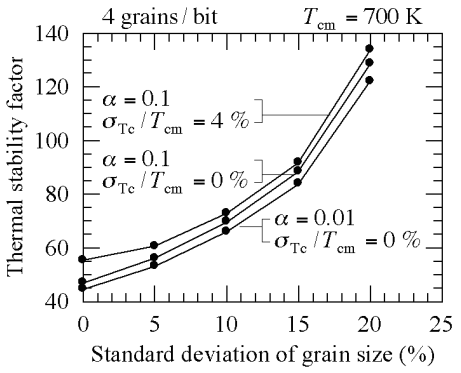

Fig. 2 Thermal stability factor required for 10 years of archiving as a function of the standard deviation of the grain size for various damping constants α and standard deviations of Curie temperature σ_{Tc}/T_{cm}.

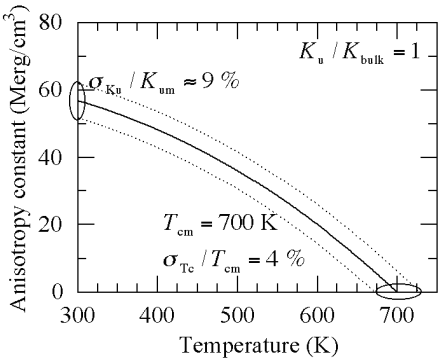

Fig. 3 Temperature dependence of anisotropy constant for standard deviation of Curie temperature σ_{Tc}/T_{cm} = 4 %.

The storage temperature and the storage time were 300 K and 10 years, respectively. The signal threshold was 0.5, and the calculation bit number was 10^7. The thermal stability factor $K_{um}V_m/kT$ and the anisotropy constant ratio K_u/K_{bulk} were evaluated for a bit error rate of 1E-3. We assumed that the grain size distribution was log-normal with a standard deviation of σ_D, and that the Curie temperature distribution was normal with a mean Curie temperature and standard deviation of T_{cm} and σ_{Tc}, respectively.

Figure 2 shows $K_{um}V_m/kT$ needed for 10 years of archiving as a function of σ_D/D_m for various α and σ_{Tc}/T_{cm} values under the conditions of 4 grains/bit and T_{cm} = 700 K. The $K_{um}V_m/kT$ value is strongly dependent on σ_D/D_m. However, $K_{um}V_m/kT$ is weakly dependent on α and σ_{Tc}/T_{cm}. When the error is low, Eq. (1) can be approximated as Eq. (12).

$$P \approx f_0 t \exp\left(-\frac{K_u V_m}{kT} \cdot \left(\frac{D}{D_m}\right)^2\right). \qquad (12)$$

The variables in an exponential function become parameters with a strong impact on bit error rate. Therefore, σ_D/D_m has a strong effect.

On the other hand, α is only related to the attempt frequency f_0, and so a difference of even 10 times α, namely f_0 has little effect on $K_{um}V_m/kT$ needed for 10 years of archiving as shown in Fig. 2 since f_0 is not an exponential variable. Therefore, α has only a weak effect, and some change in f_0 by changing T_c, T, K_u/K_{bulk}, or n also has little effect on $K_{um}V_m/kT$. Therefore, f_0 can be treated as a constant in this paper. Furthermore, from Eq. (12), time t as well as f_0 is a parameter with little impact on bit error rate.

The existence of σ_{Tc}/T_{cm} = 4 %[11] also has only a weak effect on the bit error rate as shown in Fig. 2. This is explained using the temperature dependence of K_u as shown in Fig. 3. When σ_{Tc}/T_{cm} is 4 %, the standard deviation of the anisotropy constant σ_{Ku}/K_{um} is 9 % at 300 K. The σ_{Ku}/K_{um} value of 9 % corresponds to σ_D/D_m of only 4.6 % in Eq. (12) since the changes in K_u and D caused by σ_{Ku} and σ_D correspond to $K_u = K_{um} - \sigma_{Ku}$ and $D^2 = (D_m - \sigma_D)^2$ in Eq. (12), respectively. Therefore, even for the same numerical values of σ_{Ku}/K_{um} and σ_D/D_m, σ_{Ku}/K_{um} has little apparent effect.

Next, we discuss $K_{um}V_m/kT$ for various grain numbers per bit using Fig. 4. The dependence of $K_{um}V_m/kT$ on σ_D/D_m weakens as the grain number per bit increases due to a statistical problem. If one bit contains many grains, the bit error rate becomes low since the probability is very low for a simultaneous error for more than half of the grains in one bit. For example, when there are 9 error-free grains and 7 grains with errors, the bit is error free for 16 grains/bit as shown in Fig. 5 (a). However, 2 bits are error free and 2 bits have errors when there are 4 grains/bit even with the same grain magnetization arrangement as shown in Fig. 5 (b). Thus, $K_{um}V_m/kT$ decreases as the grain number per bit increases due to a statistical problem.

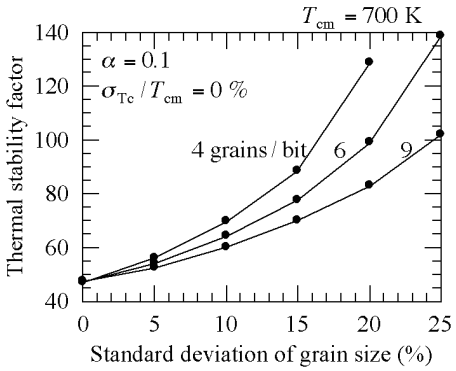

Fig. 4 Thermal stability factor necessary for 10 years of archiving as a function of the standard deviation of the grain size for various grain numbers per bit.

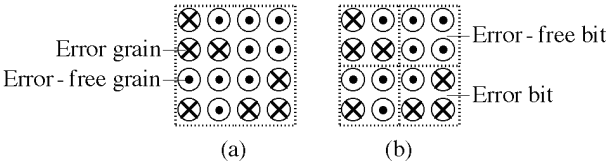

Fig. 5 (a) One bit of 16 grains/bit and (b) four bits of 4 grains/bit.

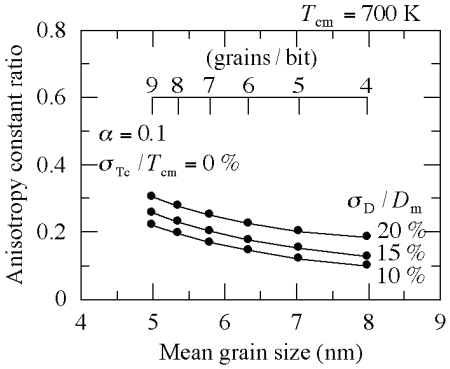

Fig. 6 Anisotropy constant ratio necessary for 10 years of archiving as a function of the mean grain size for various standard deviations of grain size σ_D/D_m.

Figure 6 shows K_u/K_{bulk} necessary for 10 years of archiving as a function of D_m for various σ_D/D_m values. The inserted scale indicates the grain number per bit corresponding to D_m for a recording density of 2 Tbpsi. Although $K_{um}V_m/kT$ decreases as the grain number per bit increases, a larger K_u/K_{bulk} is necessary as the grain number per bit increases due to the smaller grain size.

The K_u value at a storage temperature of 300 K is important as regards information stability for 10 years of archiving. And $K_u(T = 300\ \mathrm{K})$ is a function of T_c as shown in Fig. 7. The $K_u(T = 300\ \mathrm{K})$ value for a medium with a low T_c is intrinsically low. Therefore, a larger K_u/K_{bulk} is necessary for a low T_c medium to obtain the same $K_u(T = 300\ \mathrm{K})$ value as that for a high T_c medium.

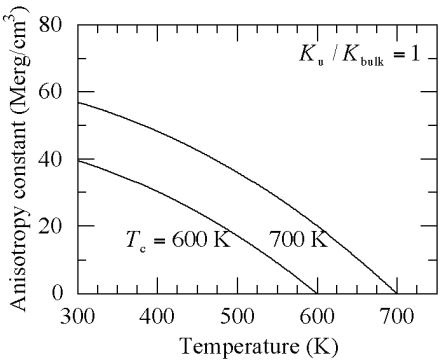

Fig. 7 Temperature dependence of anisotropy constant for Curie temperatures T_c = 600 and 700 K.

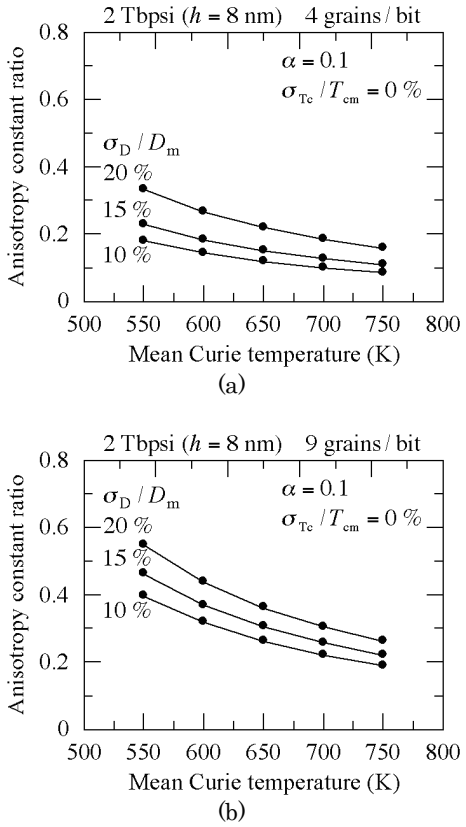

Fig. 8 Anisotropy constant ratio necessary for 10 years of archiving as a function of the mean Curie temperature for (a) 4 and (b) 9 grains/bit.

The K_u/K_{bulk} value for 10 years of archiving as a function of T_{cm} is shown in Fig. 8. As expected from the above discussion, a larger K_u/K_{bulk} is required as the mean Curie temperature decreases. A low Curie temperature is advantageous for writing in HAMR. However, it is disadvantageous for media manufacturing. For 9 grains/bit, as shown in Fig. 8 (b), a larger K_u/K_{bulk} is necessary than for 4 grains/bit as shown in Fig. 8 (a) due to the smaller grain size. The results are for a grain height h of 8 nm. If h = 4 nm, namely half the height, the K_u/K_{bulk} value must be double. The required K_u/K_{bulk} value exceeds 1.0 for the combination of 2 Tbpsi, 9 grains/bit, T_{cm} = 550 K, σ_D/D_m = 20 %, and h = 4 nm even using an FePt

medium with a large K_u.

Table 2 Calculation conditions for temperature dependence of bit error rate.

Recording density (Tbpsi)	2
Non-magnetic spacing Δ (nm)	1
Grain height h (nm)	8
Grain number (grains/bit)	4
Gilbert damping constant α	0.1
Mean Curie temperature T_{cm} (K)	700
Standard deviation of Curie temp. σ_{Tc}/T_{cm} (%)	0
Signal threshold	0.5
Bit number (bits)	10^7

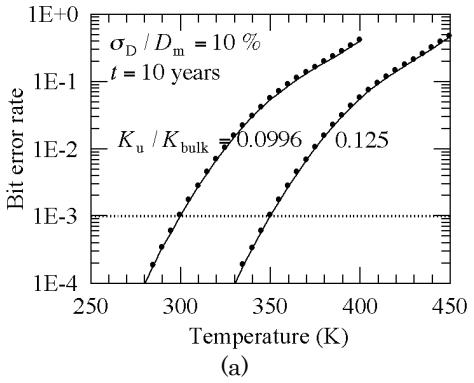

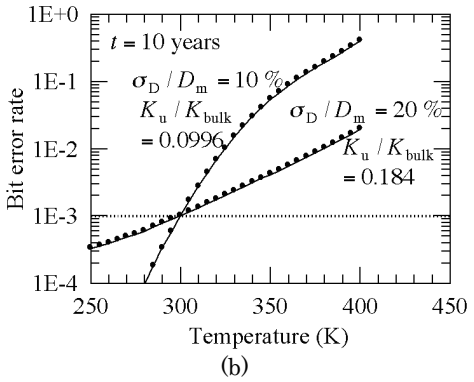

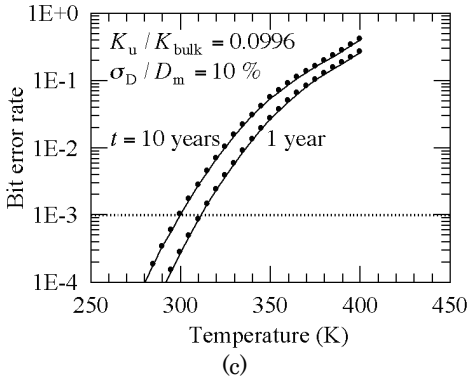

Fig. 9 Temperature dependence of bit error rate for (a) various anisotropy constant ratios K_u/K_{bulk}, (b) various standard deviations of grain size σ_D/D_m, and (c) various times t.

3.2 Temperature dependence of bit error rate

The storage temperature is also a parameter with a strong impact since temperature is a variable of an exponential function in the grain error probability as shown in Eq. (12). Therefore, we discuss the temperature dependence of the bit error rate in this section. The calculation conditions are summarized in Table 2.

Figure 9 (a) shows the temperature dependence of the bit error rate for K_u/K_{bulk} = 0.0996 and 0.125. When K_u/K_{bulk} = 0.0996, the bit error rate is 1E-3 at 300 K for 10 years. However, the bit error rate increases rapidly as the temperature increases, and it exceeds 1E-2 at only 325 K. The maximum ambient temperature of a hard disk drive appears to be about 330 K. Therefore, K_u/K_{bulk} = 0.0996 is insufficient. If K_u/K_{bulk} = 0.125, the information is stable up to 350 K when we take a certain margin for temperature into account.

When σ_D/D_m increases from 10 % to 20 %, the temperature dependence of the bit error rate weakens as shown in Fig. 9 (b). However, K_u/K_{bulk} = 0.184 is necessary for σ_D/D_m = 20 % if we are to obtain the same bit error rate for σ_D/D_m = 10 % at 300 K.

The storage time t is a weak impact parameter, and so the difference between the temperatures with a bit error rate of 1E-3 for t = 1 and 10 years is about 10 K as shown in Fig. 9 (c).

4. Conclusion

We evaluated the thermal stability factor $K_{um}V_m/kT$ and the anisotropy constant ratio K_u/K_{bulk} required for 10 years of archiving in heat-assisted magnetic recording of 2 Tbpsi employing a bit error rate calculation using the grain error probability under the conditions used in this paper. We classified the calculation parameters as those with a strong and a weak impact on the bit error rate.

The Gilbert damping constant and the Curie temperature variation are weak impact parameters. The attempt frequency can be treated as a constant.

On the other hand, the grain size variation, the grain number per bit n, the mean Curie temperature T_{cm}, and the storage temperature T are strong impact parameters.

The $K_{um}V_m/kT$ value is strongly dependent on the standard deviation of the grain size σ_D/D_m. Although $K_{um}V_m/kT$ decreases as n increases due to a statistical problem, a larger K_u/K_{bulk} is necessary as n increases due to a smaller grain size.

A larger K_u/K_{bulk} is also necessary as T_{cm} decreases. The required K_u/K_{bulk} value exceeds 1.0 for the combination of 9 grains/bit, T_{cm} = 550 K, σ_D/D_m = 20 %, and a grain height of 4 nm even using an FePt medium.

The bit error rate increases rapidly as T increases, and a certain K_u/K_{bulk} margin is required as regards temperature.

Acknowledgement We acknowledge the support of the Advanced Storage Research Consortium (ASRC), Japan.

References

1) S. H. Charap, P. -L. Lu, and Y. He: *IEEE Trans. Magn.*, **33**, 978 (1997).
2) T. Kobayashi, T. Kitayama, and Y. Fujiwara: *J. Magn. Soc. Jpn.*, **36**, 282 (2012).
3) Y. Isowaki, T. Kobayashi, and Y. Fujiwara: *J. Magn. Soc. Jpn.*, **38**, 1 (2014).
4) E. D. Boerner and H. N. Bertram: *IEEE Trans. Magn.*, **34**, 1678 (1998).
5) T. Kobayashi, Y. Isowaki, and Y. Fujiwara: *J. Magn. Soc. Jpn.*, **39**, 8 (2015).
6) T. Kobayashi, Y. Nakatani, and Y. Fujiwara: *J. Magn. Soc. Jpn.*, **42**, 110 (2018).
7) M. Mansuripur and M. F. Ruane: *IEEE Trans. Magn.*, **MAG-22**, 33 (1986).
8) J. -U. Thiele, K. R. Coffey, M. F. Toney, J. A. Hedstrom, and A. J. Kellock: *J. Appl. Phys.*, **91**, 6595 (2002).
9) Y. Nakatani, Y. Uesaka, N. Hayashi, and H. Fukushima: *J. Magn. Magn. Mat.*, **168**, 347 (1997).
10) D. A. Garanin and O. Chubykalo-Fesenko: *Phys. Rev. B*, **70**, 212409 (2004).
11) T. Kobayashi, Y. Nakatani, and Y. Fujiwara: *J. Magn. Soc. Jpn.*, **43**, 70 (2019).

Received Jul. 6, 2019; Accepted Aug. 22, 2019

J. Magn. Soc. Jpn., **43**, 120-124 (2019)

<Paper>

Perpendicular magnetic anisotropy in full-Heusler Co_2FeSi alloy and MgO bilayers

Y. Takamura, Y. Stutler, E. Matsushita, K. Shinohara, T. Suzuki, and S. Nakagawa

Dept. of Electrical and Electronic Engineering, School of Eng., Tokyo Institute of Technology, *2-12-1 Ookayama, Meguro-ku, Tokyo 152-8552, Japan*

We systematically investigated perpendicular magnetic anisotropy (PMA) in bilayers comprising ultrathin full-Heusler Co_2FeSi (CFS) alloy and MgO as an insulator. The MgO layer was fabricated using two different sputtering techniques: reactive sputtering and radio-frequency sputtering. The characteristics of the layers fabricated using the different methods were compared. Irrespective of the MgO fabrication technique, the CFS/MgO bilayers exhibited PMA when the CFS surface was exposed to oxygen, which resulted in additional Fe–O bonds at the interface. Additionally, we characterized PMA in the bilayers while varying the substrate temperature T_S for CFS sputtering. CFS samples that were 0.6-nm thick exhibited PMA when they were formed at T_S as high as 300°C. The bilayer formed at 350°C exhibited in-plane magnetic anisotropy. Quantitative analysis of the magnetic anisotropy energy density revealed that the dominant magnetic anisotropy contribution in PMA differed between the bilayers formed at 300°C and 350°C. We expect these findings to be useful in the further development of high spin-polarized ferromagnetic electrodes containing PMA for next-generation spintronics devices.

Key words: Half-metallic ferromagnet, HMF, perpendicular magnetic anisotropy, PMA, full-Heusler alloys, MgO-induced magnetic anisotropy

1. Introduction

Half-metallic ferromagnet (HMF)[1)2)] thin films containing perpendicular magnetic anisotropy (PMA)[3)] are attractive as ferromagnetic materials for next-generation magnetoresistive random access memory[4)] and racetrack memory.[5)] The extremely high spin polarization in a HMF leads to highly spin-polarized electrons in such magnetoresistive devices, efficiently yielding a very large tunnel magnetoresistance (TMR) or a high spin-transfer torque (STT).[6)]

Magnetostrictive devices based on PMA exhibit features superior to those containing in-plane magnetic anisotropy (IMA) including high scalability and low energy consumption for magnetization switching.[7)] The critical current density J_{C0} for the STT-effect current-induced magnetization switching can be dramatically decreased as the thermal stability of a ferromagnetic film remains constant.

Numerous Co-based full-Heusler alloys such as Co_2FeSi (CFS),[8)–10)] Co_2MnSi (CMS),[11)12)] and $Co_2Mn_{0.5}Fe_{0.5}Si$[13)] are theoretically expected to be HMFs. Half-metallicity has been experimentally demonstrated in some of these alloys.[13)14)] However, because of the highly symmetric crystal structure, full-Heusler alloys show little crystal anisotropy. Thus, a thin film of a full-Heusler alloy has the easy axis in the plane.

Two approaches are known to induce PMA in such ferromagnetic thin films. One approach involves forming a superlattice with ultrathin layers, such as $[Co/Pt]_n$ superlattices, to yield interfacial anisotropy.[15)] We have previously reported that superlattices of ultrathin CMS and Pd layers exhibit PMA.[11)] We determined that the PMA was strongly dependent on the surface configuration and thus occurred only when the superlattices formed on the MgO(111) substrate. Although the PMA energy density was as high as values typically reported for a conventional CoFeB/MgO system,[16)] this technique is not compatible with MgO(001)-tunnel barrier technology to attain high TMR.[17)] Recently, superlattices comprising two different non-half-metallic full-Heusler alloys with (001) orientation were reported to exhibit half-metallicity with PMA.[18)]

Another approach is to form bilayers with MgO to induce interfacial PMA, similar to the effect observed in the CoFeB/MgO system.[16)] The origin of this PMA is considered to be hybridization[19)] of the Fe 3d and O 2p orbitals; this technique is therefore widely used with Fe-containing alloys, including full-Heusler alloys. Wen et al. first reported PMA in an ultrathin full-Heusler alloy/MgO bilayer with Co_2FeAl.[20)] We have also achieved MgO-interface-induced PMA for CFS,[9)10)] which is theoretically a half-metal.[21)] Many other groups have also studied MgO-induced PMA for various types of Co-based full-Heusler alloys.[22)23)]

We have thus far demonstrated PMA in CFS/MgO bilayers in which the MgO layers were formed via two different techniques: reactive sputtering from Mg metallic targets with an $Ar–O_2$ gas mixture[9)] and radio-frequency (RF) sputtering from MgO insulating targets with pure Ar gas.[10)] In the present paper, we compare these two fabrication techniques and discuss their influence on PMA. In addition, we characterized the substrate temperature dependence of the PMA for the samples with RF-sputtered MgO layers and found that the mechanism of the anisotropy differs for the samples formed at a substrate temperature T_S greater than 300°C.

2. Experimental

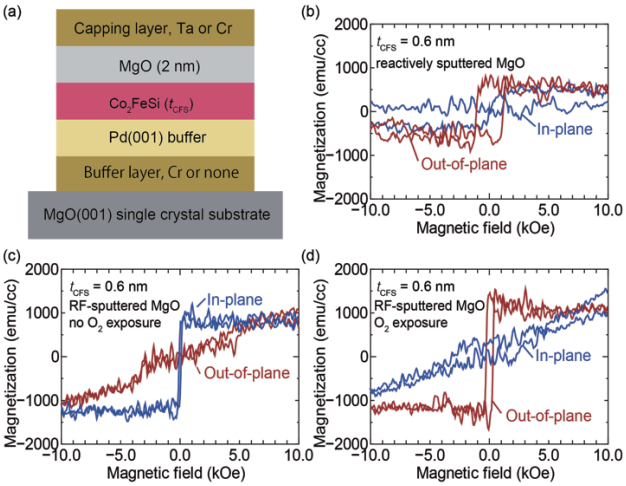

Fig. 1 (a) Schematic of a full stack of samples with a CFS/MgO bilayer. (b–d) *M*–*H* curves for CFS/MgO bilayers. The MgO layer was formed by (b) reactive sputtering and (c,d) RF sputtering. (d) The CFS surface was exposed to oxygen prior to RF sputtering of MgO layers.[9,10]

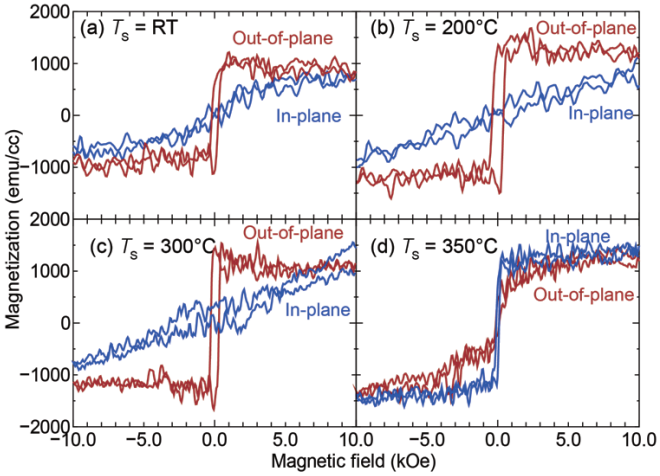

Fig. 2 *M*–*H* loops for CFS (0.6 nm)/MgO bilayers formed at (a) T_S = RT, (b) T_S = 200°C, (c) T_S = 300°C, and (d) T_S = 350°C. The MgO layers were RF sputtered and the surface of CFS was exposed to an oxygen atmosphere.

2.1 Fabrication method

We used a facing target sputtering system equipped with multi sputtering sources and a load-lock chamber to fabricate all of the samples. The base pressure of the sputtering chamber was 10^{-4} Pa. All of the samples were prepared on MgO single crystal substrates with (001) orientation.

A stack of samples is illustrated in Fig. 1(a). Ultrathin CFS and MgO bilayers were formed on (001)-oriented Pd layers. CFS layers were deposited from stoichiometric targets with dc plasma with pure Ar gas. MgO layers were formed either via reactive sputtering from Mg metallic targets at 0.13 Pa in Ar and an O_2 gas mixture with approximately O_2 1% or via RF sputtering from MgO targets at 0.13 Pa in pure Ar. The T_S during CFS was 300°C unless otherwise noted. The MgO layers were formed at room temperature (RT) and capped with either Ta or Cr layers to prevent degradation in the environment.

2.2 Characterization method

Crystallographic properties were characterized by X-ray diffraction. The chemical composition was measured by inductivity coupled plasma optical emission spectrometry (ICP-OES). Magnetic properties were characterized with a vibrating sample magnetometer.

3. Results and Discussion

3.1 Basic characterization of CFS layers

The chemical composition of the sputtered CFS layers was 52 at.% Co, 25 at.% Fe, and 23 at.% Si, which were slightly off-stoichiometric because the sputtering efficiency varies by element. The thick (~30 nm) CFS layers formed at T_S = RT and 200°C on the Pd(001) buffer layers had the *B*2 structure, as indicated by the appearance of (200) diffraction peaks with no (111) diffraction. When the CFS layers were formed at temperatures above T_S = 300°C, (111) diffraction peaks were observed; these layers thus had the $L2_1$ structure.[8] The saturation magnetization of a 100-nm-thick CFS film on the Pd buffer was 1100 emu/cm^3, which is very similar to the bulk value.[24]

3.2 Comparison between MgO formed by reactive sputtering and that formed by RF sputtering

Figure 1(b) and 1(c) compares *M*–*H* loops for the CFS/MgO bilayers in which the MgO layers were formed via reactive and RF sputtering, respectively. The CFS thickness was 0.6 nm. The sample whose MgO layer was reactively sputtered clearly exhibited PMA, whereas the sample with an RF-sputtered MgO layer exhibited IMA. The absence of PMA in the RF-sputtered samples is attributable to an interfacial structure with few Fe–O bonds, which resulted in much weaker interfacial anisotropy than shape magnetic anisotropy.

By comparing the fabrication procedures after the step-by-step deposition of the CFS layers, we observed that oxygen gas with a relatively high partial pressure was introduced to strike plasma for RF-sputtering Mg targets in the oxide mode prior to the sputtering. Then, to form the interface using similar procedures, we exposed the surface of the CFS layer to pure O_2 at 2 Pa for 10 min, equivalent to 9ML (mega Langmuir), before RF-sputtering. The sample prepared in conjunction with the oxygen treatment demonstrated very clear PMA, as shown in Fig. 1(d). The sample with 0.9 ML also exhibited PMA.

We also fabricated a sample with no MgO layer but with the surface exposed to oxygen as a control sample; it exhibited no PMA. This result indicates that PMA originates from the interfaces rather than from the CFS layer, which might be oxidized. The saturation magnetization M_S did not change with the oxygen

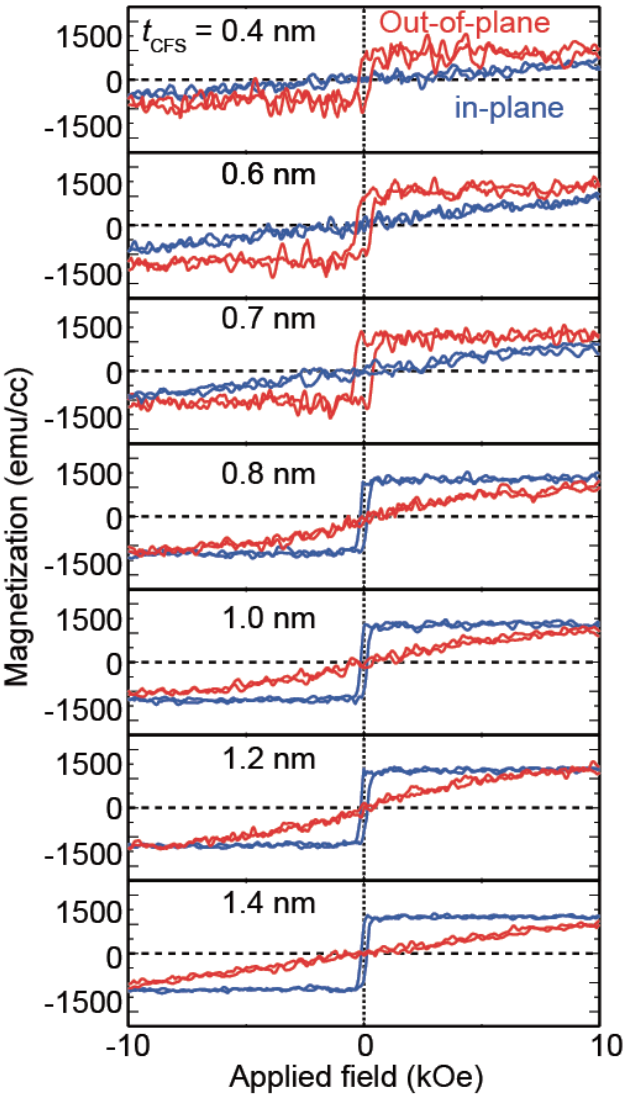

Fig. 3 Magnetization vs field curves for CFS/MgO bilayers formed at T_S = 300°C. The thickness of the CFS layers was varied from 0.4 nm to 1.4 nm.

exposure; thus, this result further suggests that the CFS was not oxidized. Only the surface can absorb oxygen to increase the number of Fe–O bonds at the CFS/MgO interface. In the thicker CFS layer, PMA disappeared, further indicating that the PMA originated at the interface. We attempted to quantitatively estimate the magnetic anisotropy energy (MAE) for these samples. However, because of the small signal-to-noise ratio, they did not give reasonable results.

3.3 Substrate temperature T_S dependence for the RF-sputtered sample

The dependence of T_S on the magnetic anisotropy is characterized in this section. The T_S was varied from RT to 350°C. The *M*–*H* curves for the CFS/MgO bilayers with various T_S are summarized in Fig. 2. Robust PMA was obtained over a wide T_S range between RT and 300°C. By contrast, the PMA disappeared in the sample formed at T_S = 350°C; the M_S was almost constant over the investigated T_S range.

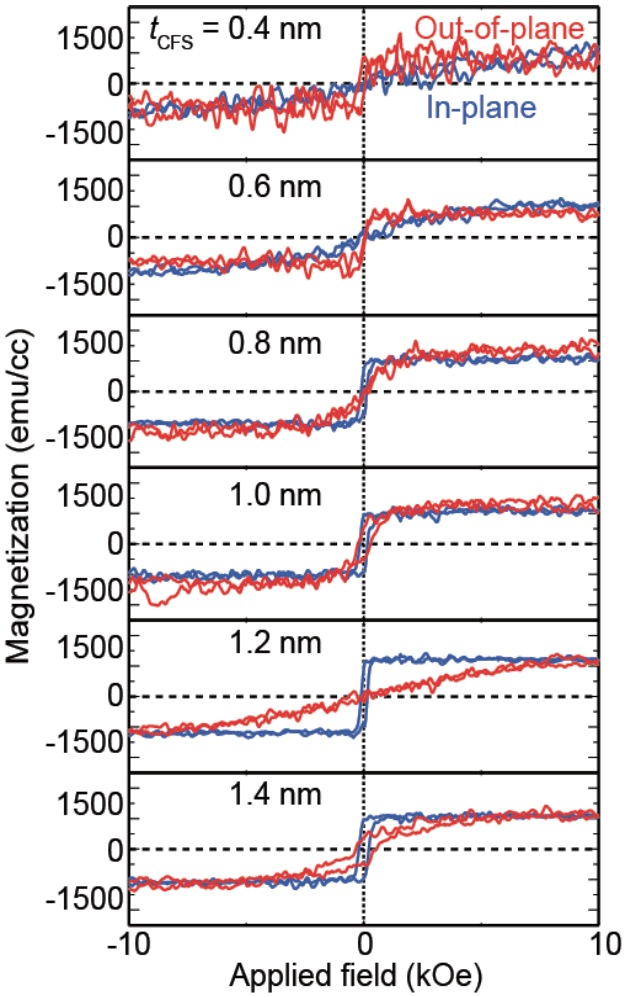

Fig. 4 Magnetization vs field curves for CFS/MgO bilayers formed at T_S = 350°C. The thickness of the CFS layers were varied from 0.4 nm to 1.4 nm.

Higher-temperature processes enable the formation of CFS layers with greater crystallinity; such layers are expected to exhibit greater spin polarization. To understand the change in the sample formed at T_S = 350°C, we further varied the thickness of the CFS layers for T_S = 300°C and 350 °C.

Figures 3 and 4 show *M*–*H* loops for CFS/MgO bilayers formed at T_S = 300°C and 350°C with various CFS thickness. For the T_S = 300°C samples, *M*–*H* loops with a high squareness ratio were observed between t_{CFS} = 0.4 nm and 0.7 nm. For the samples with $t_{CFS} \geq$ 0.8 nm, the easy axis was the in-plane direction. This change dramatically occurred when t_{CFS} was increased from 0.7 nm to 0.8 nm. We evaluated several samples and observed that this behavior was reproducible. The samples formed at T_S = 350°C exhibited PMA when t_{CFS} was less than 0.6 nm. Furthermore, thicker films exhibited in-plane anisotropy. Although the thickness range over which the CFS/MgO bilayers exhibited PMA was approximately the same, magnetic hysteresis loops for the samples prepared at T_S = 350°C changed gradually, whereas those for samples prepared at T_S = 300°C changed sharply.

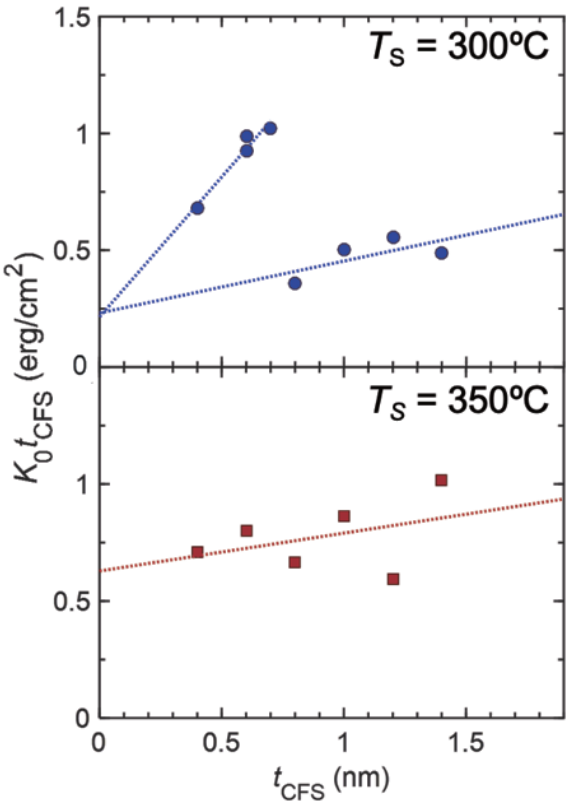

Fig. 5 K_0 t_{CFS} as a function of t_{CFS}.

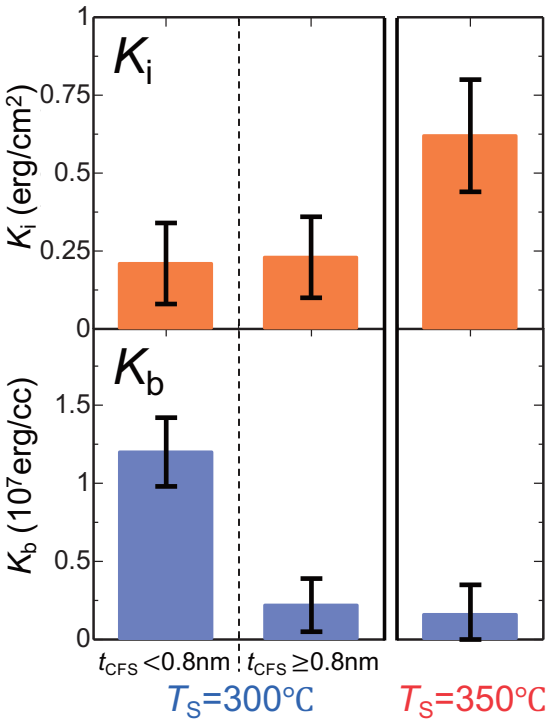

Fig. 6 Interfacial magnetic anisotropy K_i and film-originated magnetic anisotropy K_b extracted from the fitting.

3.4 Quantitative evaluation for T_S = 300°C and 350°C samples

We quantitatively analyzed the MAE in the samples from the *M*–*H* curves corresponding to the hard axis. The total of MAE, K_{tot}, is expressed as $K_0 - 2\pi M_S^2$, where K_0 is the uniaxial MAE in a bilayer and $2\pi M_S^2$ is the demagnetization energy in the CGS system of units. K_0 including interfacial PMA was further recorded as the following equation:[16]

$$K_0 t_{CFS} = K_i + K_b t_{CFS} \quad \cdots (1)$$

where K_i is the interfacial MAE and K_b is the MAE of bulk CFS. Using this equation, we separately analyzed the contribution from the interface and that from the film itself.

Figure 5 shows the product of K_0 and t_{CFS} as a function of t_{CFS}. The top and bottom panels correspond to T_S = 300°C and 350°C, respectively. When T_S = 300°C, $K_0 t_{CFS}$ increased between 0.7 nm and 0.8 nm. In the other t_{CFS} range, $K_0 t_{CFS}$ proportionally increased with increasing t_{CFS}, as expressed in Eq. 1. For the sample formed at T_S = 350°C, $K_0 t_{CFS}$ well followed Eq. 1 and no jump was observed. Interestingly, the slope for the both series of samples was positive, indicating that the films in such an ultrathin range may exhibit uniaxial anisotropy in the out-of-plane direction.

The fitting results are summarized in Fig. 6. For the samples formed at T_S = 300°C, K_i did not change before and after the jump, whereas K_b increased more than fourfold by thinning t_{CFS}. However, the K_i of the samples formed at 350°C was much larger and the K_b was the same as that corresponding to T_S = 300°C with $t_{CFS} \geq 0.8$ nm.

The aforementioned results indicate that the structure of the CFS layers with $t_{CFS} < 0.7$ nm formed at T_A = 300°C might differ from that of the thicker CFS layers and might not have the $L2_1$ structure. This structural change, which might be caused by epitaxial stress, may lead to disruption of the half-metallicity. Demonstrating the half-metallicity in this ultrathin region would require further optimization of the buffer or capping layer.[25] In contrast, when the CFS layers were formed at T_S = 350°C, K_b did not change even in the ultrathin region; the K_b also matched that of the layers formed at T_S = 300°C. These results demonstrate that the structure near the interfaces is identical to that far from the interface, which was the $L2_1$ structure. Another important finding is that the contribution of the magnetic anisotropy in the film itself was out-of-plane. This new anisotropy might be induced by elastic stress[26] and warrants further investigation.

Summary

PMA in bilayers composed of ultrathin full-Heusler CFS alloy and MgO were systematically investigated. The CFS/MgO bilayers with RF-sputtered and reactively sputtered MgO layers were compared. Both techniques led to CFS/MgO bilayers with PMA, but oxygen exposure of the CFS surface was required to form the CFS/MgO

interface.

In addition, we characterized the PMA while varying the T_S for CFS sputtering. Robust PMA was observed at temperatures as high as T_S = 300°C. PMA in the sample formed at T_S = 350°C behaved differently when the thickness of the CFS layers was varied. Quantitative analysis of MAE density revealed that the interface and bulk contribution were dominant in the bilayers formed at 300°C and 350°C, respectively. Our findings should be useful in the further development of half-metallic ferromagnetic electrodes with PMA for next-generation spintronics devices.

Acknowledgements This work was supported by JSPS KAKENHI Grant Number 25889021, Kato Foundation for Promotion of Science, and Kenjiro Takayanagi Foundation. ICP-OES measurements were performed by the Ookayama materials analysis division, Technical Department, Tokyo Institute of Technology. The authors would like to thank MARUZEN-YUSHODO Co., Ltd. (http://kw.maruzen.co.jp/kousei-honyaku/) for the English language editing.

References

1) R.A. de Groot, F.M Muller, P.G. Van Engen, K.H.J. Buschow: *Phys. Rev. Lett.*, **50**, 2024 (1983).
2) J.H. Park, E. Vescovo, H.J. Kim, C. Kwon, R. Ramesh, T. Venkatesan: *Nature*, **392**, 794 (1998).
3) H. Ohmori, T. Hatori, S. Nakagawa: *J. Appl. Phys.*, **103**, 07A911 (2008).
4) D. Shum, et al.: *2017 Symposium on VLSI Technology*, Kyoto, Japan, T208 (2017).
5) S.S.P. Parkin, M. Hayashi, L. Thomas: *Science* **32**, 190 (2008).
6) L. Thomas, et al.: *J. Appl. Phys.*, **115**, 172615 (2014).
7) A.D. Kent, *Nature Mater.*, **9**, 699 (2010).
8) Y. Takamura, R. Nakane, S. Sugahara: *J. Appl. Phys.*, **105**, 07B109 (2009).
9) Y. Takamura, T. Suzuki, Y. Fujino, S. Nakagawa: *J. Appl. Phys.*, **115**, 17C732 (2014).
10) K. Shinohara, T. Suzuki, Y. Takamura, S. Nakagawa: *AIP Advances*, **8**, 055923 (2018).
11) N. Matsushita, Y. Takamura, Y. Fujino, Y. Sonobe, S. Nakagawa: *Appl. Phys. Lett.*, **106**, 062403 (2016).
12) H. Liu, Y. Honda, T. Taira, K. Matsuda, M. Arita, T. Uemura, M. Yamamoto: *Appl. Phys. Lett.,* **101**, 132418 (2012).
13) Y. Sakuraba, M. Ueda, Y. Miura, K. Sato, S. Bosu, K. Saito, M. Shirai, T. Konno, K. Takanashi: *Appl. Phys. Lett.*, **101** 2442-R (2012).
14) R. Shan, H. Sukegawa, W.H. Wang, M. Kodzuka, T. Furubayashi, T. Ohkubo, S. Mitani, K. Inomata, K. Hono: *Phys. Rev. Lett.*, **102**, 246601 (2009).
15) S. Maat, K. Takano, S.S.P. Parkin, E.E. Fullerton: *Phys. Rev. Lett.,* **87**, 087202 (2001).
16) S. Ikeda, K. Miura, H. Yamamoto, K. Mizunuma, H.D. Gan, M. Endo, S. Kanai, J. Hayakawa, F. Matsukura, H. Ohno: *Nature Mater.*, **9**, 721 (2009).
17) S. Yuasa, T. Nagahama, A. Fukushima, Y. Suzuki, K. Ando: *Nature Mater.*, **3**, 868 (2004).
18) T.L. Brown-Heft, J.A. Logan, A.P. McFadden, C. Guillemard, P.L. Fèvre, F. Bertaran, S. Andrieu, C.J. Palmstrøm: *Phys. Rev. Mater.*, **2**, 034402 (2018).
19) J. Okabayashi, J.W. Koo, H. Sukegawa, S. Mitani, Y. Takagi, T. Yokoyama: *Appl. Phys. Lett.*, **105** 122408 (2014).
20) Z. Wen, H. Sukegawa, S. Mitani, K. Inomata: *Appl. Phys. Lett.*, **98**, 242507 (2011).
21) P. Bruski, S.C. Erwin, M. Ramsteiner, O. Brandt, K.-J. Friedland, R. Farshchi, J. Herfort, H. Riechert: *Phys. Rev. B*, **83**, 140409(R) (2011).
22) T. Kubota, T. Kameda, J. Kim, A. Tsukamoto, S. Takahashi, Y. Sonobe, K. Takanashi: *Mater. Trans.*, **57**, 773 (2016).
23) Y. Jin, S. Valloppilly, P. Kharel, R. Pathak, A. Kashyap, R. Skomski, D.J. Sellmyer: *J. Phys. D,* **52**, 035001 (2019).
24) S. Wurmehl, G.H. Fecher, H.C. Kandpal, V. Ksenofontov, C. Felser, H.-J. Lin, J. Morais: *Phys. Rev. B*, **72**, 184434 (2005).
25) Y. Iida, J. Okabayashi, S. Mitani: *Appl. Phys. Lett.*, **113**, 252401 (2018).
26) S.C. Wu, G.H. Fecher, S.S. Naghavi, C. Felser: *J. Appl. Phys.*, **125**, 082523 (2019).

Received Feb. 18, 2019; Revised Jul. 29, 2019; Accepted Sep. 11, 2019

J. Magn. Soc. Jpn., **43**, 125-132 (2019)

<Paper>

Improving Transmission Efficiency with Magnetic Coating Technology for Lightweight Wireless Power Transfer Coil Using Aluminum Plate

S. Endo, M. Sato, Y. Bu, and T. Mizuno
Department of Engineering, Shinshu University, *4-17-1 Wakasato, Nagano, Nagano, Japan*

To improve the fuel efficiency of electric vehicles, it is necessary to reduce the weight of the wireless power transfer coil in the vehicles. Resistance due to the skin effect or the proximity effect increases during wireless power transfer, decreasing the transmission efficiency. This study aims to reduce the weight of the coil by replacing it with an aluminum plate coil, which is easy to manufacture and inexpensive. The weight of the coil was reduced by 3/4 (from 1.9 to 0.44 kg) when compared with copper Litz wire. Furthermore, the AC resistance was reduced by applying magnetic coating to the same coil. Consequently, the transmission efficiency increased from 88.2% to 89.3%, an improvement of 1.1%. The optimal material for magnetic coating was revealed in an analysis.

Keywords: wireless power transmission, aluminum plate, lightweight, low cost, high efficiency, copper loss reduction, magnetic composite material, magnetic coating technology

1. Introduction

As a power supply method for electric vehicles (EVs), wireless power transmission is attracting attention because it allows to charge stationary EVs seamlessly and is not associated with cable-related problems such as forgetting to charge or leakage[1-3]. Wireless power transmission for EVs operates at a high frequency of 85 kHz. Since a high-frequency loss typically occurs in wireless power transfer coils[4], the litz copper wire (LCW) with good high-frequency characteristics is generally used in wireless power transfer coils for EVs[5-11].

To improve the fuel efficiency of EVs, a weight reduction of the embedded coil is highly desirable. Furthermore, a coil that is inexpensive and easy to manufacture is required.

To meet these requirements, we examined a relatively facile fabrication of a coil using an aluminum plate. However, the aluminum plate (AP) coil has a large AC resistance due to the proximity effect[12]. At the same time, this resistance can be reduced by coating the coil with a magnetic layer[13-15]. Therefore, we coated the AP coil with a magnetic composite material using a low-loss amorphous alloy powder achieving a magnetically coated plate (MCP) coil.

In this study, the optimal magnetic composite material was analyzed using the finite element method (FEM). Furthermore, the impedance characteristics of the coil were evaluated, and the transmission efficiencies of the AP and MCP coils were measured using the double-LCC resonant circuit.

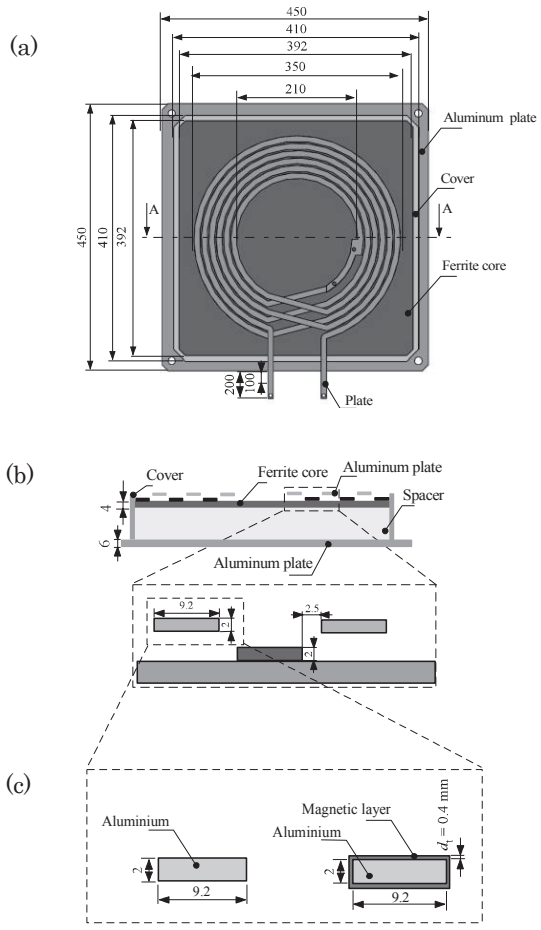

Fig. 1 Structure of the aluminum plate (AP) and magnetically coated plate (MCP) coils (unit: mm): (a) plane view and (b) sectional view. (c) Structure of the AP and MCP.

2. Structure of the Wireless Power Transfer Coil

2.1 Structure of the aluminum plate coil

Figure 1 illustrates the structure of the AP and MCP receiving-side coils in planar (Figure 1(a)) and sectional (Figure 1(b)) views. A ferrite core in the back yoke improves the inductance, while an AP on the back surface of the coil provides magnetic shielding[16]. Figure 1(c) depicts the structures of the AP and MCP used for the coil. The AP has a width of 9.2 mm, a thickness of 2 mm, and a conductor cross section of A = 18.4 mm^2. A brush was used to apply the magnetic composite material to the AP, and the thickness of the magnetic layer of the resulting MCP was 0.4 mm.

2.2 Structure of the receiving-side litz copper wire coil

Figures 2(a) and 2(b) illustrate the planar and sectional views of the LCW coil structure, respectively. The coil has a short spiral coil structure with an outer diameter of 350 mm and the number of turns N = 6 wound in parallel.

Figure 2(c) illustrates the cross-sectional structure of the litz wire used in the coil. Generally, the LCW has a conductor diameter of 0.2 mm with a 0.02-mm thick insulating film and a final diameter of 7.4 mm. The number of strands n was 1176, while the conductor cross section was A = 36.8 mm^2.

2.3 Structure of the power transmission coil

Figures 3(a) and 3(b) illustrate the planar and sectional views of the power transfer coil structure, respectively. The transfer coil used in this study, standardized by SAE, is a rectangular spiral coil containing the same litz wire as the LCW coil[4].

Figure 3(c) illustrates the cross-sectional structure of the litz wire used in the coil. Generally, the LCW has a conductor diameter of 0.049 mm with a 5.5-μm thick insulating film and a final diameter of 5.0 mm. The number of strands n was 4200, and the conductor cross section was A = 7.92 mm^2.

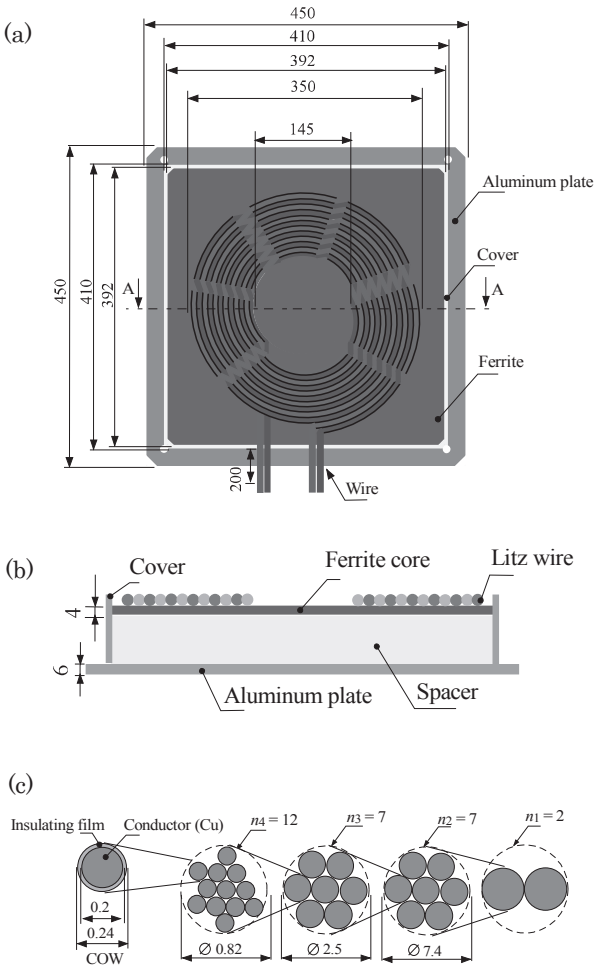

Fig. 2 Structure of the litz copper wire (LCW) coil (unit: mm): (a) plane view and (b) sectional view. (c) Structure of the LCW.

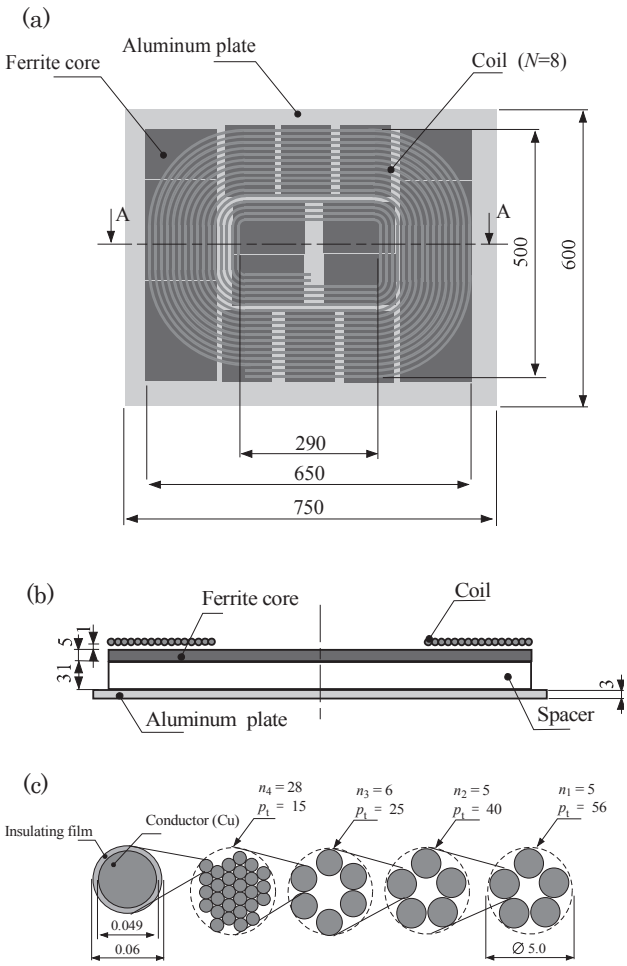

Fig. 3 Structure of power transmission coil (unit: mm). (a) Plane view. (b) Section A-A. (c) Wire structure of power transmission coil (n = 4200, A = 7.9 mm^2).

3. Analysis of the Wireless Power Transfer Coil

Figure 4 shows the results of the FEM-based analysis exhibiting the MCP coil characteristics with respect to permeability (μ). AC magnetic field analysis (Ansys Maxwell 2D) was performed, and the coil resistance R and inductance L were calculated. The quality factor Q of the MCP coil was calculated according to Eq. (1). The transmission efficiency of the MCP coil η_C was calculated from the kQ product using Eq. (2)[17].

$$Q = \frac{\omega L}{R} \tag{1}$$

$$\eta_c = \frac{(kQ)^2}{\left(1+\sqrt{1+(kQ)^2}\right)^2} \times 100 \quad (\%) \tag{2}$$

Figure 4(a) depicts the trend associated with the resistance of the coil. As μ' improves, the resistance decreases. This is because the induced magnetic flux of the magnetic layer of the coil is increased, while the proximity effect is reduced. Moreover, the resistance decreases due to the decrease in μ''. This is because the iron loss decreased.

Figure 4(b) shows the inductance of the coil. An increase in μ' improves the inductance, whereas no effect is observed due the variations in μ''. As μ' increases, the flux generated by the coil is confined inside the coil; hence, the flux linkage increases and the inductance improves. μ'' does not affect the distribution of the magnetic flux or the inductance.

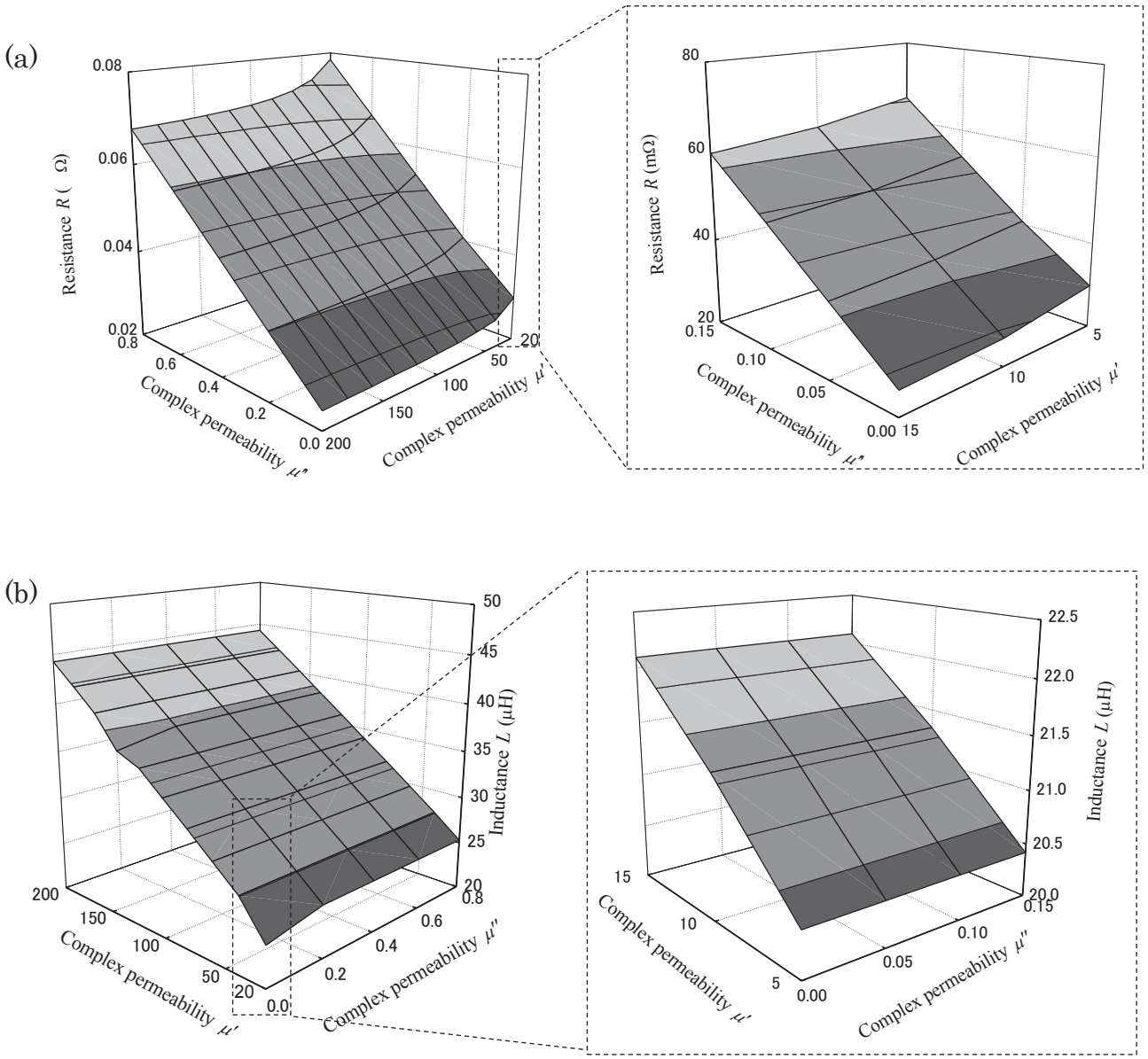

Fig. 4 Characteristics of the MCP coil with respect to permeability. (a) Resistance R. (b) Inductance L.

Figure 5(a) shows the quality factor Q of the coil. As μ'' increases, the Q decreases. In contrast, when μ' increases, the Q increases. Q decreases as R increases and improves as L increases. Figures 4(a) and 4(b) demonstrate that Q has changed under the impact of R and L.

Figure 5(b) shows the coupling coefficient k. A trade-off can be observed between μ' and k. As μ' increases, the coupling coefficient $k$decreases because the magnetic flux linking the power transfer coil to the MPC coil decreases. μ'' does not affect the distribution of the magnetic flux or the coupling coefficient k.

Figure 5(c) shows the transmission efficiency between the coils, η_C. While the quality factor Q is improved due to the increase in μ', the improvement in the efficiency of the material of high permeability is low because the coupling coefficient k decreases. However, the efficiency improvement is large in this case since μ'' does not affect the coupling coefficient k. Therefore, the use of a low-loss magnetic material is optimal because the impact of μ'' on the efficiency is larger than that of μ'.

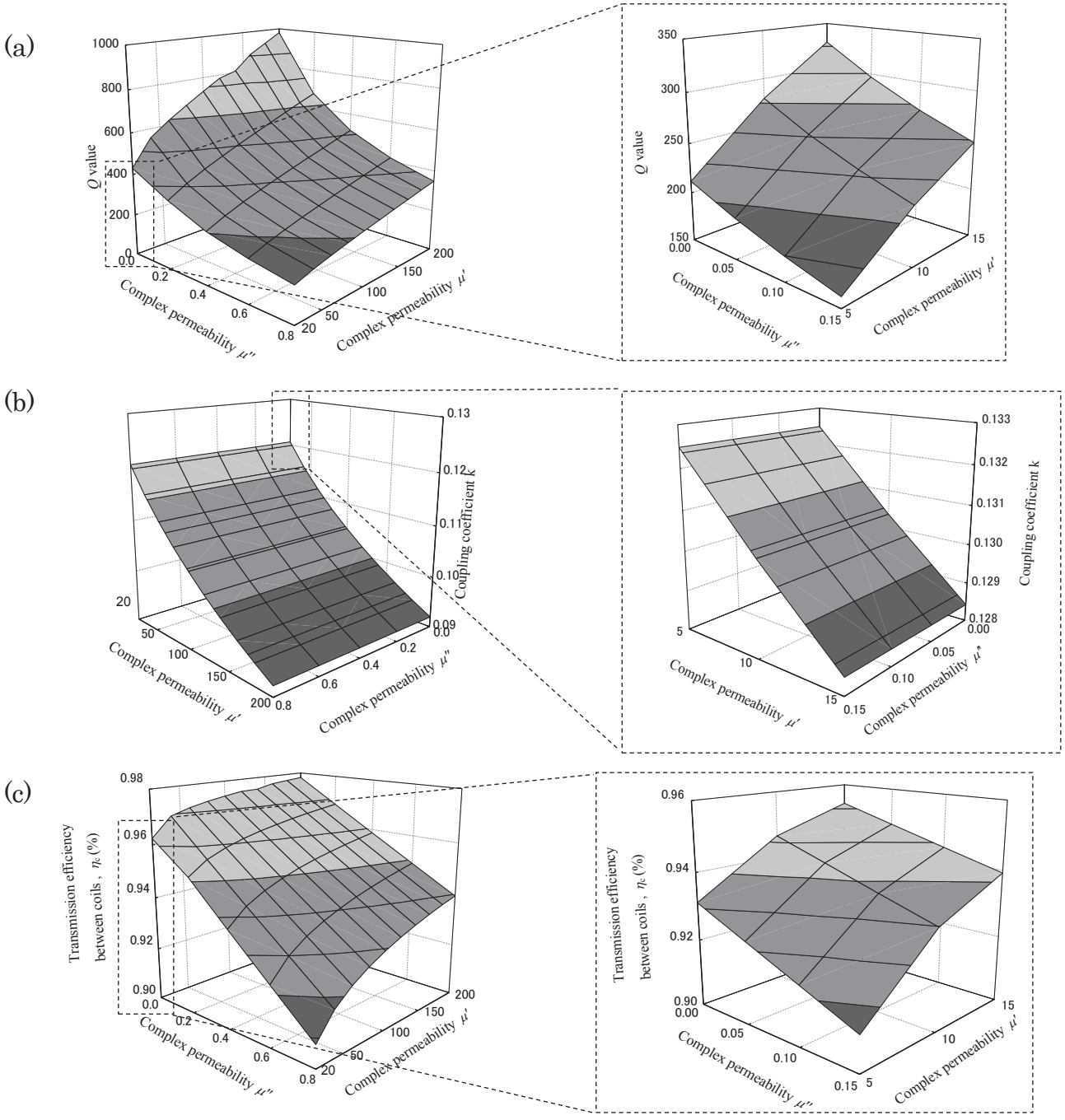

Fig. 5 Characteristics of the MCP coil with respect to permeability. (a) Quality factor Q. (b) Coupling coefficient k. (c) Transmission efficiency between coils, η_C.

Table 1 Specification of the magnetic material.

		Amorphous metal
Volume filling rate		57 Vol%
Mean diameter D_{50}		2.6 μm
Saturation magnetization B_s		0.80 T
Complex permeability	μ' (f= 85 kHz)	10.3
	μ'' (f= 85 kHz)	0.082

Table 1 lists the characteristics of the magnetic material used for magnetic coating. A magnetic composite material, in which an amorphous alloy powder and a silicone adhesive were mixed, was used as the magnetic material[18]. The ratio of the magnetic powder to the silicone adhesive in the magnetic composite material was defined as the volume filling rate, which was 57 Vol%. The amorphous alloy contained a spherical powder with a diameter of 2.6 μm. A vibrating sample magnetometer (VSM, Riken Denshi) was employed for measuring saturation magnetization B_S. A B-H analyzer (IWATSU, SY-8218) was used to measure the magnetic permeability. A low-loss magnetic composite material was used for magnetic coating.

4. Characterization of the Manufactured Coil

4.1 Coil impedance characteristics and transmission efficiency

Figure 6 shows the characteristics of the manufactured coil. An impedance analyzer was used for conducting the measurements. The inter-coil efficiency was calculated according to Eq. (2). The coupling coefficient k was calculated from the mutual inductance M product using Eq. (3). The mutual inductance M was calculated from the inductance L_a and the antiphase inductance L_b in the in-phase series using Eq. (4).

$$k = \frac{M}{\sqrt{L_1 L_2}} \tag{3}$$

$$M = \frac{L_a - L_b}{4} \quad \text{(H)} \tag{4}$$

Here, L_1 denotes the transfer coil inductance (H), L_2 denotes the receiving coil inductance (H), Q_1 denotes the transfer coil quality factor, and Q_2 denotes the receiving coil quality factor.

Figure 6(a) shows the resistance of the manufactured coil. As the frequency increases, the skin effect and proximity effect increase resulting in the increase in the AC resistance. Wireless power transmission for EVs uses the 85 kHz band as the frequency. The magnetic coating reduced the resistance from 85.7 mΩ to 66.9 mΩ.

Figure 6(b) shows the inductance of the manufactured coil. The inductance is not affected by the frequency. The magnetic coating increased the inductance from 21.3 μH to 22.1 μH. The inductance of the MCP coil was 22.1 μH and that of the LCW coil was 15.1 μH. Note that the LCW coil had a smaller inner diameter compared to that of the AP coil and had a low inductance.

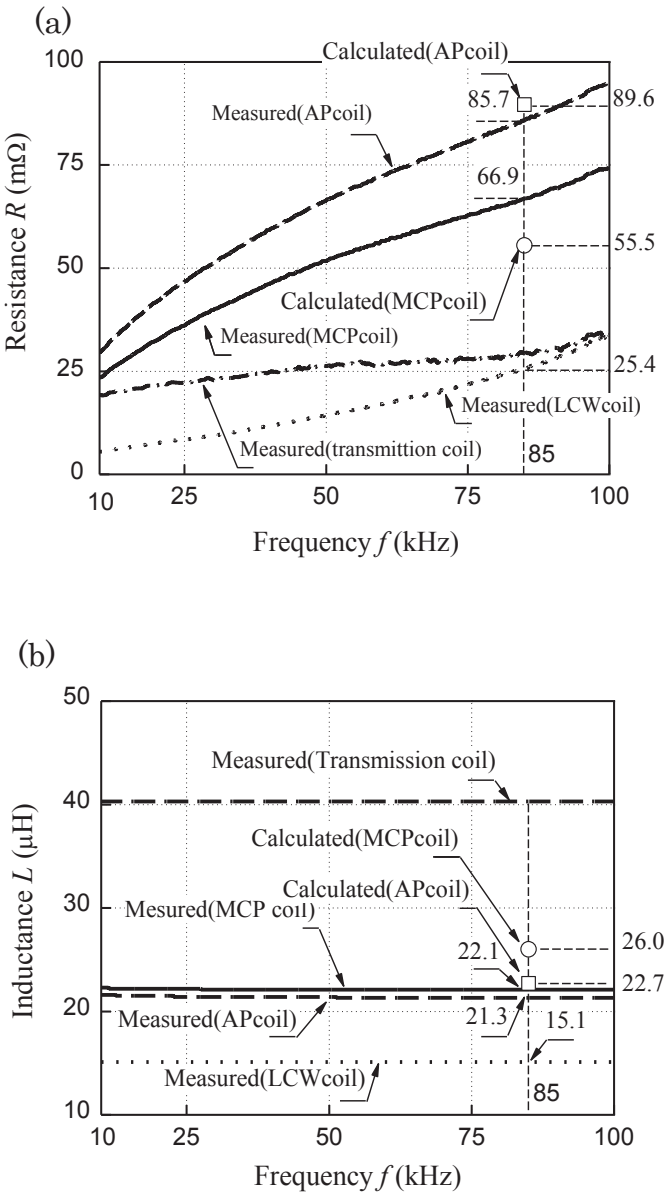

Fig. 6 Characteristics of manufactured coil. (a) Resistance R. (b) Inductance L.

Figure 7(a) shows the quality factor Q of the manufactured coil. The frequency of the quality factor is characterized by a curve that peaks at a specific value. The peak value is determined by the coil structure. Magnetic coating increased the quality factor at 85 kHz from 135 to 176.

Figure 7(b) shows the coupling coefficient k of the manufactured coil. The coupling coefficient is not affected by the frequency. Magnetic coating reduced the coupling coefficient at 85 kHz from 0.161 to 0.151.

Figure 7(c) shows the transmission efficiency between the coils. Magnetic coating improved the efficiency at 85 kHz by 0.3%.

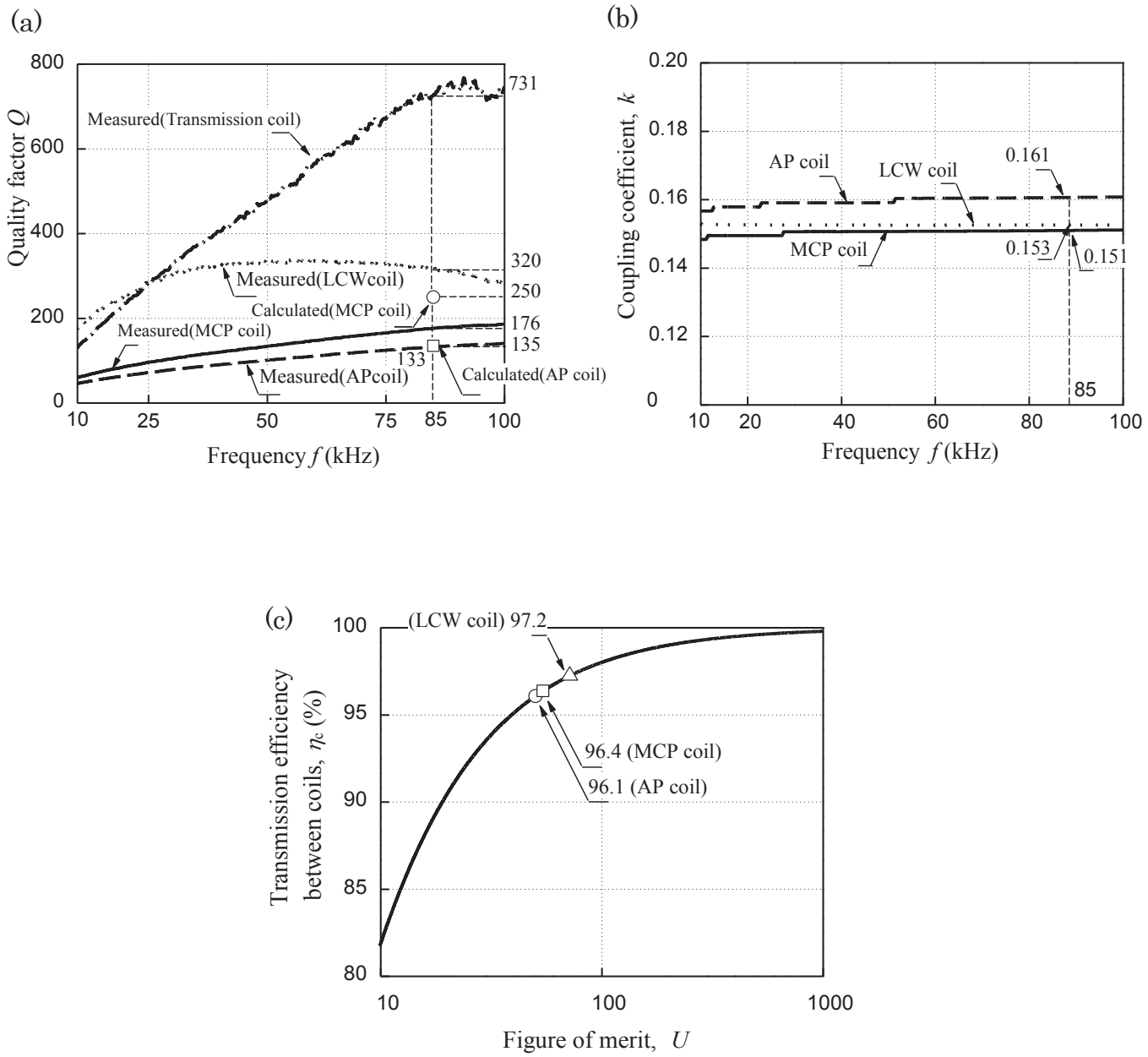

Fig. 7 Characteristics of manufactured coil. (a) Quality factor Q. (b) Coupling coefficient k. (c) Transmission efficiency between coils, η_C.

4.2 Wireless power transfer experiment

Figure 8 shows the circuit of a wireless power transmission system using the double-LCC method[19-20].

Figure 9(a) shows the transmission efficiency η_{DC}, which is indicative of the coil frequency characteristics (Eq. 5). Measurements were performed using a power analyzer (YOKOGAWA, WT 1800).

$$\eta_{DC} = \frac{P_o}{P_i} \times 100 \quad (\%) \tag{5}$$

As shown in Figure 9(a), the maximum value η_{DCmax} of the transmission efficiency using the AP coil at the transmission distance l = 150 mm and the output power P_{out} = 1 kW was 87.7% at the frequency f = 84 kHz. The η_{DCmax} values were 89.0% at f = 84 kHz for the MCP coil and 89.0% for the LCW coil at f = 87 kHz.

As depicted in Figure 9(b), the transmission efficiencies η_{DC} of the AP, MCP, and LCW coils were 88.2%, 89.3%, and 89.4%, respectively, at an output power P_o = 3 kW. Hence, the magnetic coating of AP improved the transmission efficiency η_{DC} by 1.1%. The difference between the transmission efficiencies η_{DC} of the MCP coil and the LCW coil was 0.1%, which implies an unaltered transmission efficiency.

4.3 Wireless power transfer coil mass

Figure 10 denotes the mass of the manufactured coil. The total masses of the AP, MCP, and LCW coil devices were 7.69 kg, 7.84 kg, and 9.3 kg, respectively. This translates to a mass reduction of 17.3% for the AP coil and 15.7% for the MCP coil compared to that the mass of the LCW coil.

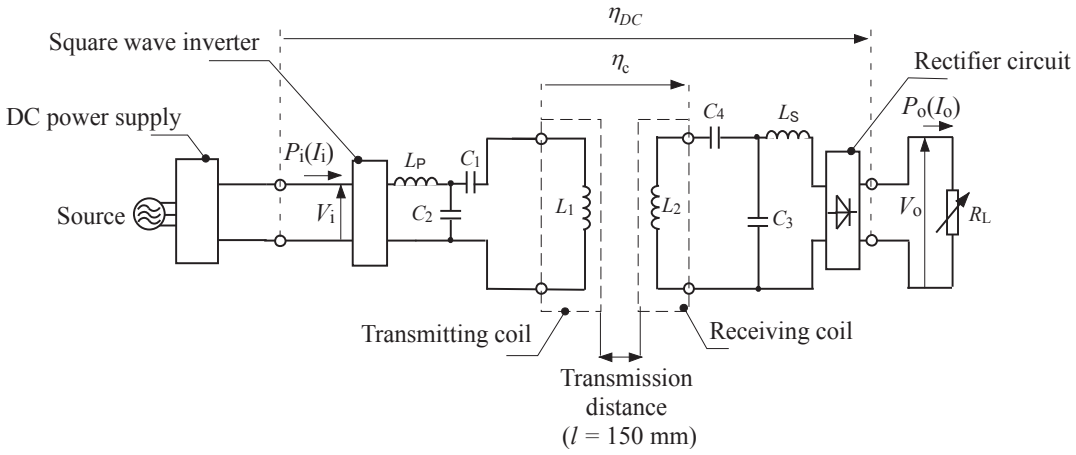

Fig. 8 Circuit for wireless power transmission (f = 85 kHz).

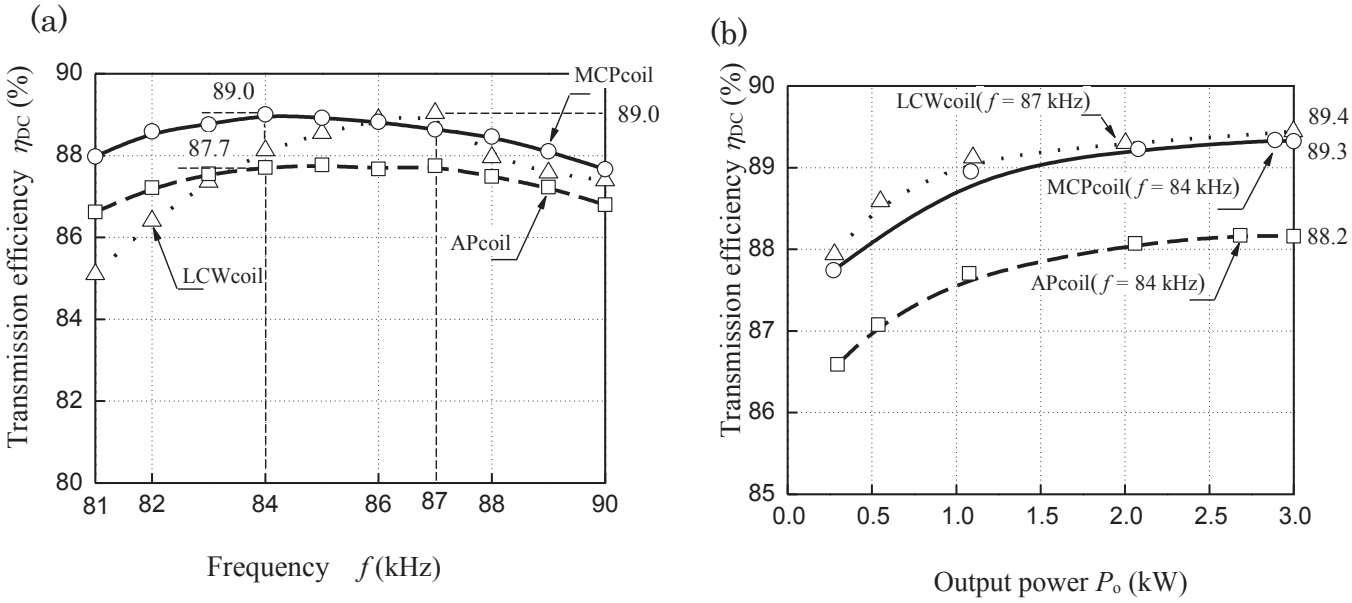

Fig. 9 Characteristics of the manufactured coil. (a)Efficiency η_{DC} vs. frequency characteristics (l = 150 mm, P_o = 1 kW). (b) Output power vs.frequency characteristics (l = 150 mm).

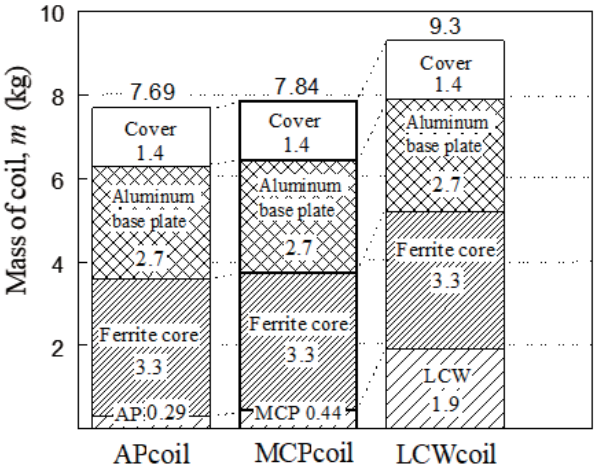

Fig. 10 Mass of the wireless power transfer coil.

The masses of the coils alone were 0.29 kg, 0.44 kg, and 1.9 kg for the AP, MCP, and LCW coils, respectively. Hence, the respective masses of the AP and MCP coils were approximately 1/6 and 1/4 that of the LCW coil. Therefore, the MCP coil is considered to be advantageous because it is lightweight, easy to manufacture, and does not impede the performance.

5. Conclusion

FEM-based analysis revealed that the use of low-loss magnetic materials is optimal for magnetic coating.

A magnetic coating made of a magnetic composite material using a low-loss amorphous alloy powder allowed to reduce the resistance of the tested coil from 85.7 mΩ to 66.9 mΩ. The transmission efficiency at 3 kW transmission improved by 1.1% compared to the transmission efficiency of the AP coil.

The transmission efficiencies of the LCW and MCP coils were observed to be equal. The mass of the MCP coil was 1/4 that of the LCW coil. Therefore, the MCP coil can be considered to be advantageous because it is lightweight, easy to manufacture, and does not impede the performance.

References

1) T. Imura, H. Okabe, and Y. Hori: *Proc. 2009 IEEE Vehicle Power and Propulsion Conference*, Dearborn, Michigan, Sep. 7, 2009, pp. 936-942 (2009).
2) K. Throngnumchai, T. Kai, and Y. Minagawa: *Proc. 2011 IEEE Energy Conversion Congress and Exposition*, Phoenix, Arizona, Sep.16, 2011, pp. 843-849 (2011).
3) C. Qiu, K. T. Chau, C. Liu, and C. C. Chan: *Proc. 2013 World Electric Vehicle Symposium and Exhibition (EVS27)*, Barcelona, Spain, Nov.17, 2013, pp.1-6 (2013).
4) *Wireless Power Transfer for Light-Duty Plug-in/Electric Vehicles and Alignment Methodology*, pp.82-84 (Society of Automotive Engineers, Inc., United States of America, 2019).
5) D. Barth, B. Klaus, and Thomas Leibfriend: *Proc. 2017 IEEE Wireless Power Transfer Conference (WPTC)*, Taipei, Taiwan, May.10, 2017, pp.1-6 (2017).
6) C. R. Sllivan: *IEEE Transactions on Power Electronics.*, **16**, 281 (2001).
7) R. P. Wojda, and M. K. Kazimierczuk: *IET Power Electronics.*, **5**,257 (2012).
8) R. P. Wojda, and M. K. Kazimierczuk: *IEEE Transactions on Industry Applications.*, **54**, 3548 (2018).
9) J. Acero, R. Alonso, J. M. Burdio, L. A. Barragan, and D. Puyal: *IEEE Transactions on Power Electronics.*, **21**, 856 (2006).
10) C. Carretero: *IEEE Transactions on Industrial Electronics.*, **64**, 4474 (2017).
11) T. Mizuno, T. Ueda, S. Yachi, R. Ohtomo, and Y. Goto: *IEEJ Journal of Industry Applications.*, **3**, 35 (2014).
12) Y. Tang, H. Ma, D. J. Thrimawithana, and U. K. Madawala: *Proc. 2017 IEEE PELS Workshop on Emerging Technologies: Wireless Power Transfer (WoW)*, Chongqing, China, May.22, 2017, pp.167-172(2017).
13) T. Yamamoto, Y. Bu, and T. Mizuno: *IOS Press.*, **23**, 486 (2016).
14) T. Yamamoto, Y. Bu, T. Mizuno, Y. Yamaguch, T. Kano: *IEEJ Journal of Industry Applications.*, **7**, 43 (2018).
15) Y. Bu, S. Endo, T. Mizuno: *IEEE Trans. Magn.*, **54**, 8401205 (2018).
16) S. Park: *IEEE Trans. Magn.*, **54**, (2018).
17) A. Kurs, A. Karalis, R. Moffatt, J. D. Joannopoulos, P. Fisher, and M. Soljacic: *Science*, **317**, 83 (2007).
18) K. Sugimura, D. Shibamoto, N. Yabu, and T. Yamamoto., *IEEE Trans. Magn.*, **53**, (2017).
19) T. Kan, T. D. Nguyen, J. C. White, R. K. Malhan, and C. C. Mi: *IEEE Trans. Power Electron.*, **32**, 1638(2017).
20) S. Li, W. Li, J. Deng, T. D. Nguyen, C. C. Mi, *IEEE Trans. Vehicular Technology*, **64**, 2261 (2015).

Received Jul. 09, 2019; Revised Sep. 1, 2019; Accepted Sep. 19, 2019

Journal of the Magnetics Society of Japan

Vol. 43 No. 6 (通巻第 306号) 2019年11月 1 日発行

Vol. 43 No. 6 Published Nov. 1, 2019
by the Magnetics Society of Japan
Tokyo YWCA building Rm207, 1–8–11 Kanda surugadai, Chiyoda-ku, Tokyo 101–0062
Tel. +81–3–5281–0106 Fax. +81–3–5281–0107

Printed by JP Corporation Co., Ltd.
Sports Plaza building 401, 2–4–3, Shinkamata Ota-ku, Tokyo 144–0054
Advertising agency: Kagaku Gijutsu-sha

発行：（公社）日本磁気学会 101–0062 東京都千代田区神田駿河台 1–8–11 東京YWCA会館 207 号室
製作：ジェイピーシー 144–0054 東京都大田区新蒲田 2–4–3 スポーツプラザビル401 Tel.（03）6715–7915
広告取扱い：科学技術社 111–0052 東京都台東区柳橋 2–10–8 武田ビル 4F Tel.（03）5809–1132